Heartbeat Optical Coherence Tomography

Tianshi Wang

Heartbeat Optical Coherence Tomography

Optische coherentie topografie in een hartslag

Thesis

to obtain the degree of doctor from the
Erasmus University Rotterdam
by command of the Rector Magnificus

Prof.dr. H.A.P. Pols

in accordance with the decision of the Doctorate Board.

The public defense shall be held on
Tuesday 10th of March 2015 at 15.30 hours

by

Tianshi Wang
born in Liaoning, China

ERASMUS UNIVERSITEIT ROTTERDAM

Doctoral Committee

Promotor: Prof.dr.ir. A.F.W. van der Steen

Other members: Dr. E.S. Regar
                     Prof.dr. A.G.J.M. van Leeuwen
                     Prof.dr. G.J. Tearney

Copromotor: Dr. G. van Soest

Contents

Chapter 1

General introduction
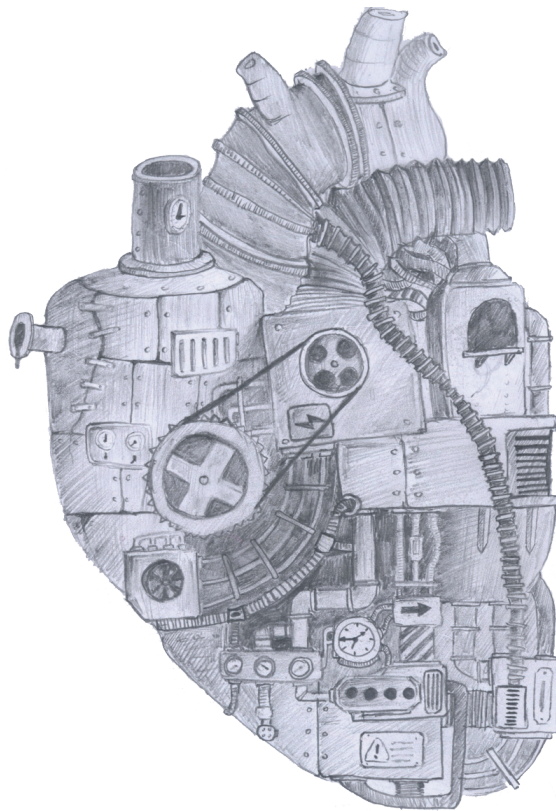
Coronary artery disease (CAD) is a manifestation of atherosclerosis, a systemic inflammatory disease of the arteries that causes the formation of plaques in the artery walls[1]. Different plaques may give rise to different symptoms: a gradual narrowing (stenosis) of the vessel by growth of a fibrous or calcific plaque will cause chest pain (due to cardiac ischemia) upon exertion, a condition called stable CAD. Sudden onset of chest pain, or chest pain at rest, is a symptom of unstable CAD or acute coronary syndrome (ACS), which is associated with thrombus formation on plaques, mostly due to rupture of a lipid-core lesion[2-4]. The most severe form of this disease may lead to a myocardial infarction or heart attack[5].

Minimally invasive treatment (percutaneous coronary intervention, PCI) is a cheap and fast clinical treatment for CAD[6,7]. Therapy of PCI for both ACS and stable CAD consists of reopening the occluded or narrowed coronary artery with a balloon followed by the placement of a metal or bioresorbable plastic stent to support the tissue. The guidance of PCI depends vitally on imaging technologies, and all stent implantations use X-ray angiography to size and position the stent. The schematic of PCI procedure is showed in Figure 1.1(a), and an example of stent implanting under the guidance of angiography is showed in Figure 1.1(b-d).
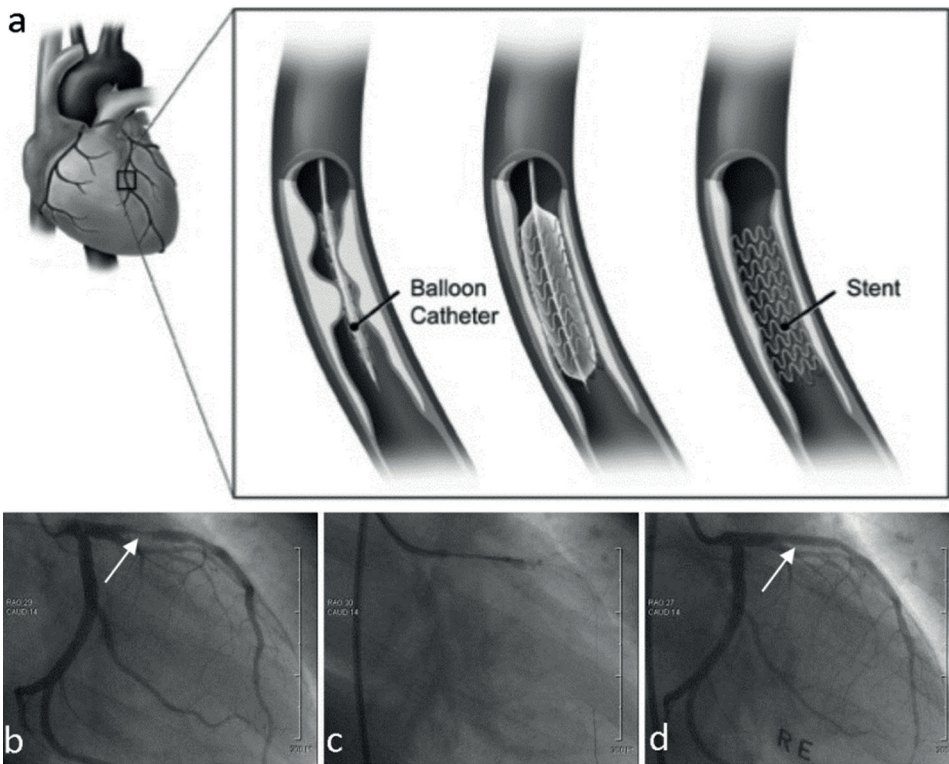
Figure 1.1 | (**a**) Schematic diagram of PCI procedure: implanting a stent to temporally open the narrowed lumen using a balloon catheter. (**b**) Angiography of an artery with a narrowed lumen. (**c**) Angiography of a balloon catheter when implanting the stent. (**d**) Angiography of the artery after the stent was implanted.

1

1.1 | Drawbacks of angiography

Angiography alone, however, does not provide all information needed to fully assess the condition of the diseased artery, and hence leaves too much room for interpretation in planning and execution of the intervention.

The drawbacks of angiography are:
– It provides a 2D projection image of a moving, 3D anatomy. This leads to ambiguity in measurements and identification of the culprit lesion.
– Visualization of the lumen only, and not the vessel wall which is the cause of the disease.
– Poor contrast, especially for thrombus and dissection, leading to ambiguity.
– X-ray exposure to the cardiologist and cath lab staff.

As a result, coronary interventions are less effective than they could be, due to inaccurate stent sizing, positioning, or expansion. Stent malapposition, dissections, over- and underexpansion may lead to delayed healing, restenosis or acute stent failure[8-11]. Adverse response of the vessel wall and atherothrombotic events have been reported as a result of interaction of a stent or balloon with a lipid-core plaque[12,13]. Several studies carried out over the past few years paint a consistent picture, showing that within 12 months after PCI, 12-15% of patients need to return to the cath lab[14-16], representing a cost to European and US societies of > 2 billion dollars per year due to repeat PCIs. These repeat interventions fall into three categories[15]: (i) staged; (ii) target lesion revascularization (TLR); and (iii) non-target lesion revascularization. Each of these categories points to shortcomings of current PCI practice: (i) part of a necessary treatment is postponed because full treatment is considered too taxing for the patient; (ii) the treatment was ineffective or caused an adverse vessel wall response; and (iii) some lesions were missed at the index procedure that became symptomatic within a year.

1.2 | Intravascular optical coherence tomography (IV-OCT)

Intravascular imaging can provide valuable images of pathophysiology and procedural boundary conditions in addition to angiography. Unlike X-ray imaging, intravascular imaging technologies actually visualize the diseased vessel wall from inside the lumen. Interventionists guided by intravascular imaging may take into account the state of the vessel wall to assess stent length and size. Intravascular imaging offers the possibility to perform tissue characterization[17,18], which is vital to understanding and anticipating the vessel response to device or medical interventions.
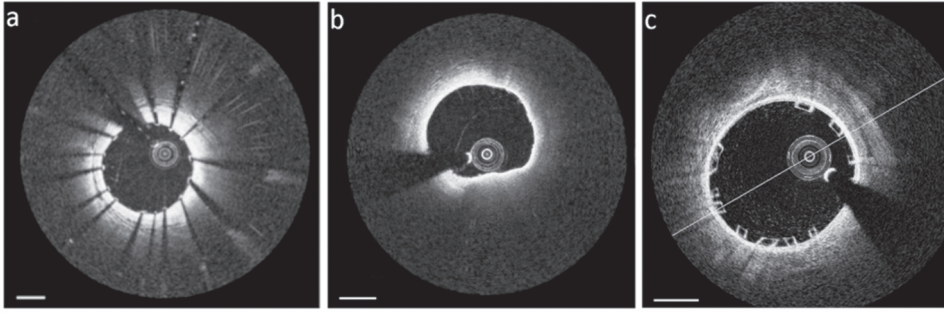
Figure 1.2 | IV-OCT images of (**a**) artery lumen with metal stent implanted, (**b**) lipid plaque (12-7 o'clock) and (**c**) artery lumen with bioresorbable vascular scaffold implanted. The scale bar is 1.0 mm.

Among several intravascular imaging techniques, intravascular optical coherence tomography (IV-OCT) is rapidly becoming the method of choice for assessment of the coronary artery wall. Based on infrared light, it provides high-resolution (20-30 μm), high-contrast image of the coronary artery wall and any implanted stents (Figure 1.2)[19-22]. Catheter-based imaging shows the free lumen without projection artifacts, but also the proximal and distal stable landing zones for a stent. This is important information that can guide the cardiologist to place a stent with better long-term outcomes.

Since the first intracoronary images in a living patient were acquired in 2001 in Boston, IV-OCT has guided over one hundred thousand PCI procedures worldwide, and generated a wealth of insights into CAD and stenting[23]. A recent analysis also suggests that PCIs guided by IV-OCT have significantly better outcome than those guided by angiography alone[24]. Figure 3 illustrates typical IV-OCT images, as acquired with a commercial system. The high resolution in the cross sectional images allow for a highly detailed assessment of vessel wall architecture, including measurement of the fibrous cap thickness[25], plaque rupture, thrombus, stent strut apposition, edge dissections, etc.

The most important current application of IV-OCT is guidance of stenting procedures. In the pre-implantation phase of the procedure, IV-OCT provides measurements of the minimal lumen area, the diameters of stable landing zones on both sides of a lesion to be stented, and the segment length between the landing zones. Moreover, IV-OCT can provide extra information of the artery that is sometime not available in angiography. Figure 1.3 shows a case of unclear culprit lesion that showed up as a normal lesion in angiography but a mural thrombus in IV-OCT.

1
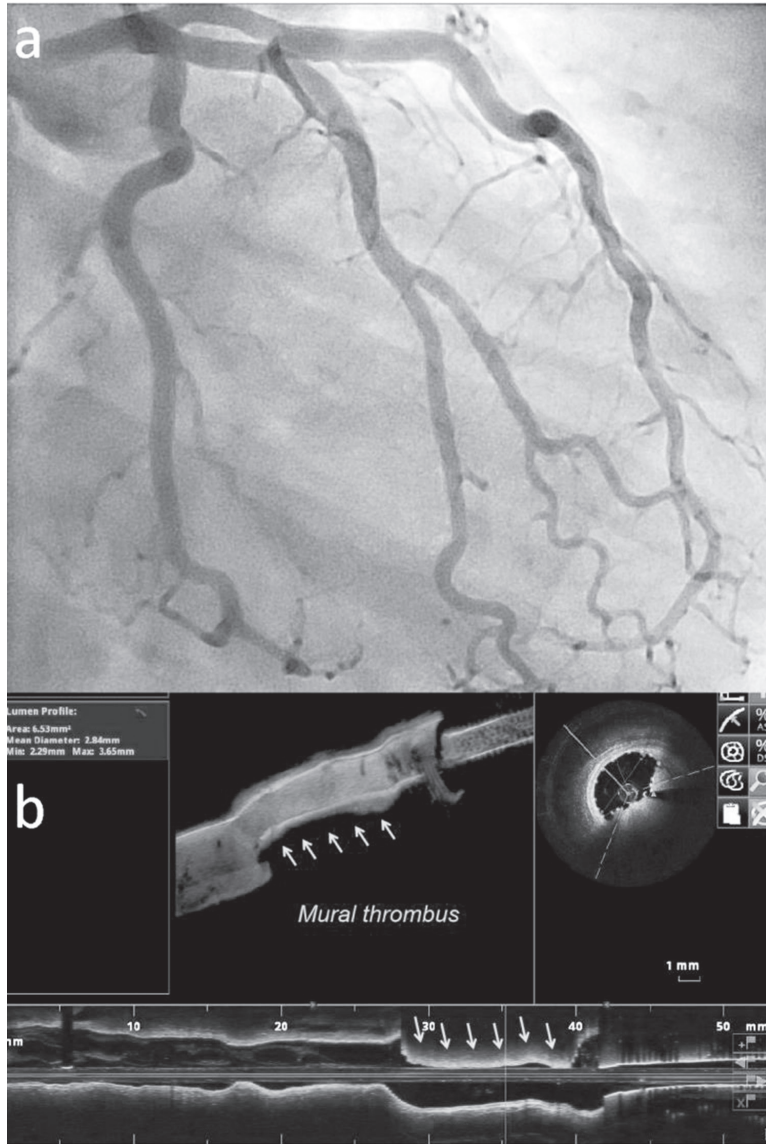
Figure 1.3 | *In vivo* (**a**) angiography and (**b**) IV-OCT images of a 40-year old female patient. The angiography of the artery looks normal. However, mural thrombus is observed in IV-OCT images. The extra information suggests implantation of stents, which cannot be provided by angiography alone.

After stent implantation, IV-OCT can be used to visualize the stent, to check if it is well-apposed to the artery wall, if significant dissections were created, presence of thrombus on the stent struts, and other procedure-related phenomena that have been related to worse outcomes[8-10]. If any are observed, the decision may be taken to post-dilate the stent with a balloon, or put in an additional stent. Figure 1.4

demonstrates an intervention in complex lesions. Under the guidance of IV-OCT, 5 stents were finally implanted inside the artery to achieve an optimal result. In addition to intervention guidance, IV-OCT also shows promise as a prognostic imaging tool with potential for imaging of vulnerable plaques – unstable lesions that may rupture and cause ACS [26].
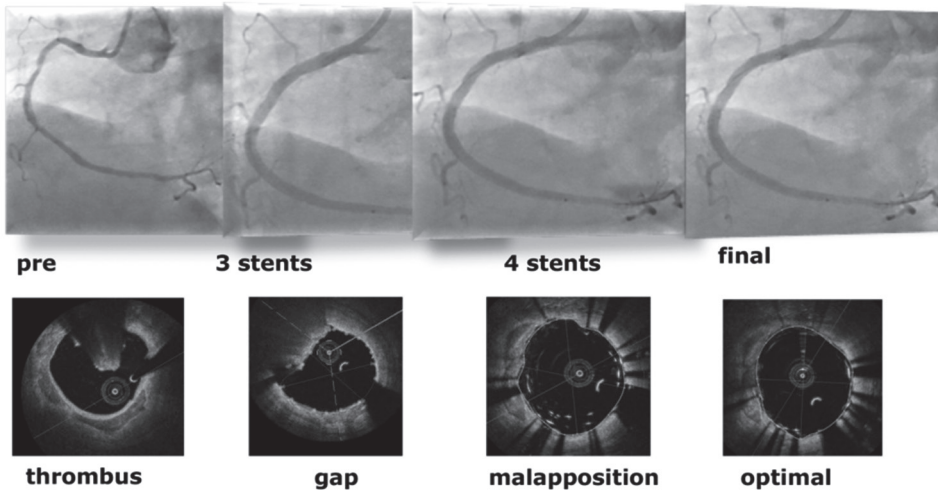
Figure 1.4 | Intervention in complex lesions for a 63 year old male patient. After three stents were implanted, a forth one was suggested because a gap between stents was observed in IV-OCT images. A fifth stent was suggested due to a malapposition observed before the optimal result was achieved.

The recent introduction of bioresorbable vascular scaffolds (BVS) further increases the utility and need for IV-OCT in PCI. These novel plastic stents provide mechanical support in the months after angioplasty, and are absorbed by the tissue in the time frame up to two years after the intervention to recreate a healthy, layered vessel wall[27]. These devices hold the promise to treat coronary artery disease effectively without leaving behind a permanent metal structure. BVS require more accuracy in sizing and implantation, however, since they have less tolerance for overexpansion. IV-OCT has been playing a key role in evaluating BVS performance *in vivo* and establishing its advantages over conventional metal stents.

1. 3 | Issues in IV-OCT

Optical Coherence Tomography (OCT) was first demonstrated in 1994 by David Huang *et al*[28]. The OCT images are constructed upon the interference pattern of the back reflecting light from both the sample arm and the reference arm. When OCT was first invented, a mechanically scanning was employed in the

reference arm to acquire the reflectivity profile of the sample (time-domain OCT; TD-OCT). The latest implementation of OCT, frequency-domain OCT (FD-OCT)[29-32] replaces such mechanically scanning by a wavelength (frequency) scanning in a laser source. A Fourier transform has to be applied additionally to generate an axial line image (A-line) as shown in Figure 1.5(b). Compared to TD-OCT, FD-OCT enables a much faster imaging speed with an improved signal-to-noise ratio[33,34]. In interventional application, an intravascular catheter is used to scan the artery wall circumferentially. In conventional intravascular catheters, the scanning takes place when a rotary junction part rotates the entire optical fiber in the catheter. A lens or mirror on the fiber tip directs the laser beam sideways toward the artery wall. The rotating fiber is pulled back inside the lumen of the artery under investigation to acquire a volumetric dataset. The schematic of conventional intravascular catheter is showed in Figure 1.5(c).
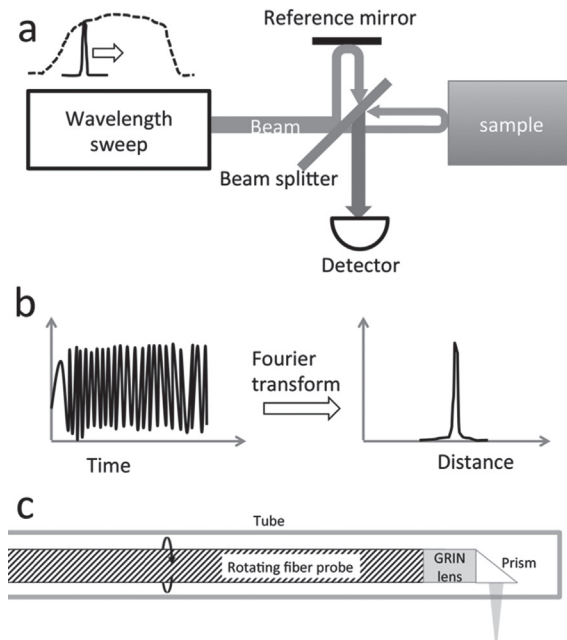
Figure 1.5 | (**a**) Schematic of Optical Coherence Tomography. (**b**) Schematic of signal processing of OCT. (**c**) Schematic of the intravascular catheter. GRIN: gradient refractive index.

1.3.1 | Non-uniform rotation distortion

Due to the torque transferring and the rotating friction of the fiber probe, non-uniform rotation distortion (NURD)[35,36] affects the image quality of IV-OCT. The artifact shows up as distortion in the images. Even worse, the NURD can cause wobbling of the entire images. Figure 1.6 demonstrates the NURD artifact in a coronary artery model. The light coupled into the rotatory junction part also becomes unstable when the scanning speed goes above 350 revolutions per s (RPS)[37].
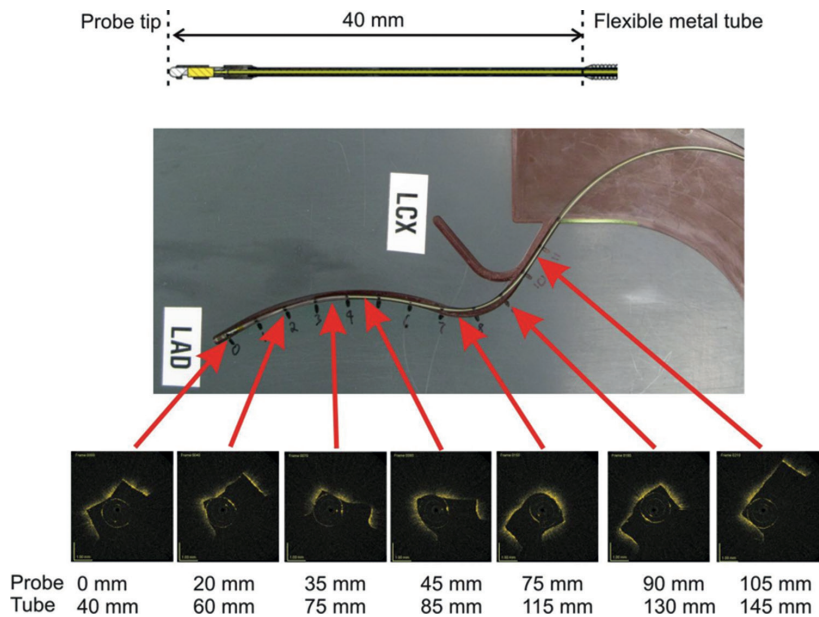
Figure 1.6 | NURD observed using the OCT intravascular imaging catheter inside the 2D coronary artery model. The optical catheter was rotating at the rate of 4 turns/s inside the sheath and pulled back from the extremity of the LAD branch (middle) along 11cm at a speed of 2mm/s. OCT images at several locations during the pullback are illustrated (bottom).

1.3.2 | Undersampling

Limited by the fundamental beam scanning modality of the catheter and the speed of the OCT engine, the fastest commercial IV-OCT system acquires 160 frames per s (fps) with 500 A-lines per image; the maximum pullback speed is 40 mm/s. In this situation, the images are under-sampled in the pullback direction: only 12% of the lumen is sampled because the image spacing ie. the spacing between two neighboring images is approximately 8 times greater than the transverse resolution (20-30μm). Consequently, the image quality of the longitudinal view is not as good as that of the cross-sectional images[38]. Figure 1.7 shows how the the image spcaing influences the longitudinal rendering.
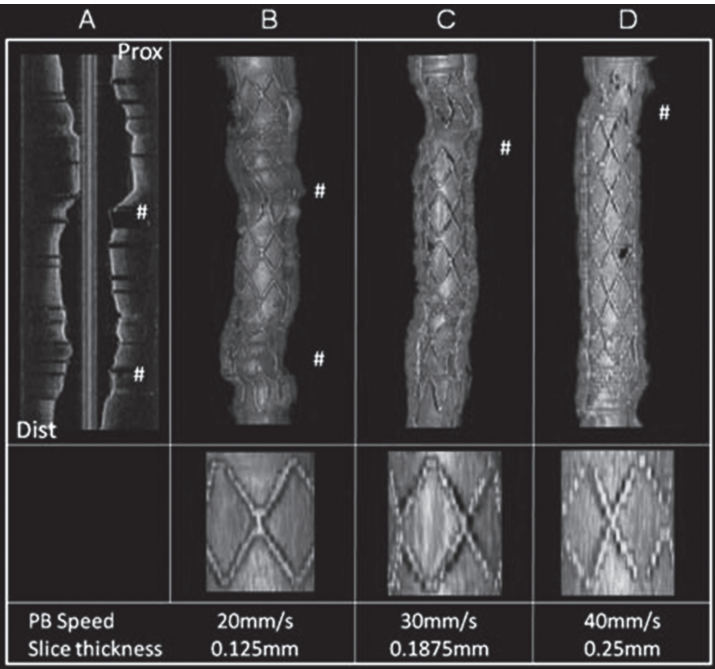
Figure 1.7 | The trade-off between pullback speed, cardiac motion artifacts, and image resolution of the three-dimensional frequency domain optical coherence tomography reconstructions: as demonstrated in a porcine model. # represents cardiac motion artifacts; (**A**) represents 2D longitudinal image; (**B-D**) represents corresponding 3D reconstructions with progressively increased pullback speeds and consequential fewer cardiac motion artifacts at the expense of a lower resolution. PB, pullback.

1.3.3 | Cardiac motion artifacts

In clinical applications, account has to be taken not only of the NURD and under-sampling but also of the cardiac motion artifact[38-40]. Due to motion of the catheter along the vessel, the cardiac motion during image acquisition will cause inaccuracy in image spacing and possibly image order. This can affect the fidelity of the longitudinal rendering and three-dimensional reconstruction of the data (Figure 1.8).

Trace of catheter tip relative to stents
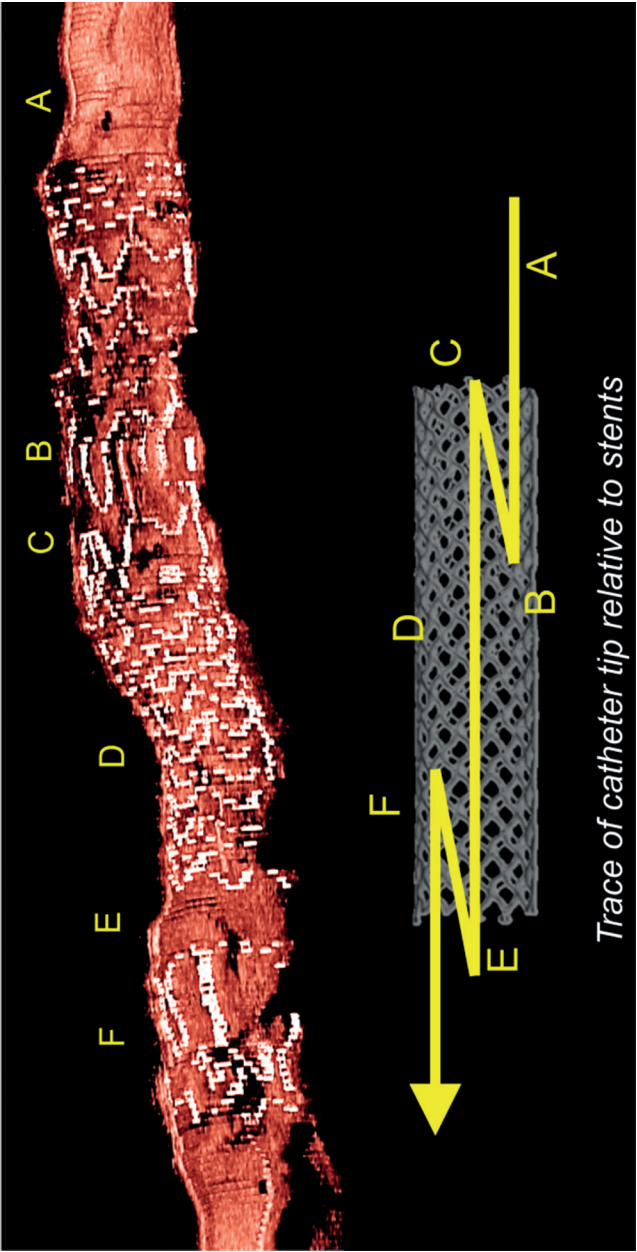
Figure 1.8 | 3D reconstruction of an *in vivo* pullback through a bio-absorbable vascular scaffold (BVS) implanted in the left anterior descending coronary artery of a 53-year old male patient. The system was imaging at 100 fps with 20 mm/s pullback speed. The scaffold appears irregular as a result of artifacts due to cardiac motion; the inset illustrates the position of the imaging tip relative to the scaffold during the pullback. Tissue motion during left ventricular contraction can be so strong that the direction of motion of the tip "reverses" relatively to the artery. At E, this even leads to an apparent gap in the stent. The blocky appearance of the stent is caused by longitudinal undersampling.

1

While the image appearance in the pane of rotation is good enough, a longitudinal section or 3D rendering shows clear artifacts due to motion and undersampling, appearing blocky and distorted. Longitudinal measurements, which are important for determining the optimal stent length, can be unreliable due to the variable pullback speed. The apparent gap in the stents showed in Fig. 1.8 may be interpreted as stent fracture and be unnecessarily remedied by placement of an additional stent. The longitudinal undersampling means that we do not actually acquire an adequately sampled 3D data set. In addition to the lack of continuity of the acquired data set, the vessel changes size due to the varying intrcoronary pressure over the cardiac cycle, and the frame-to-frame pressure differential is variable across the data set. These caliber changes cannot be corrected, even if coronary pressure were measured during acquisition. Using OCT data as the basis for imaging of tissue biomechanics, or for flow computations, is precluded because of these limitations.

1.4 | What is needed?

The artifacts due to cardiac motion and undersampling can be amended by speeding up OCT imaging acquisition, with the objective of attaining isotropically sampled, motion-free imaging of the coronary vasculature. As a solution of NURD, the beam scanning modality needs to be replaced. Therefore, to solve all these issues of IV-OCT, a new mode of performing IV-OCT needs to be developed concerning a bran-new beam scanning modality of the catheter and laser source with a promising performance at high speed.

Thesis objective and outlines

In order to overcome NURD, under sampling and cardiac motion artifacts at the same time, we propose to develop a super fast IV-OCT system, capable of providing sufficient number of frames of an artery within one cardiac cycle. This thesis demonstrates the development of a system called *Heartbeat OCT* that replies on the combination of two key components: a synchronous micro motor and a FDML laser.

Chapter 2 introduces the development of the synchronous micro motor rotating at several thousands speed. The principle of the motor is explained, and the performance of the motor is evaluated in terms of maximum speed, rotation uniformity, damping coefficient and driving torque.

Chapter 3 demonstrates the first prototype of Heartbeat OCT using the micro motor as the distal actuator and an FDML laser as the swept source. The system achieves the highest imaging speed in IV-OCT. The advantage of high imaging speed is demonstrated in the longitudinal rendering of *in vitro* images.

Chapter 4 shows the second prototype of Heartbeat OCT and its application in *in vivo* imaging. Using an improved FDML laser and a refined micro motor, the system further surpasses the record of imaging speed in IV-OCT. The value of Heartbeat OCT for *in vitro* and *in vivo* imaging is demonstrated in

various visualizations including cross-sectional image, longitudinal rendering and three-dimensional (3D) reconstruction.

Chapter 5 shows the optical analysis of astigmatism in intravascular catheters. The negative astigmatism is numerical quantified based on several catheter models. Compensation methods are proposed, analyzed and evaluated, which can facilitate the design and optimization of Heartbeat OCT.

Chapter 6 summarizes the work presented in this thesis, and discusses the future of Heartbeat OCT.

Chapter 2

Development of a high-speed synchronous micro motor and its application in intravascular imaging

Tianshi Wang, Charles Lancée, Robert Beurskens, John Meijer, Bart Knapen, Antonius F. W. van der Steen and Gijs van Soest
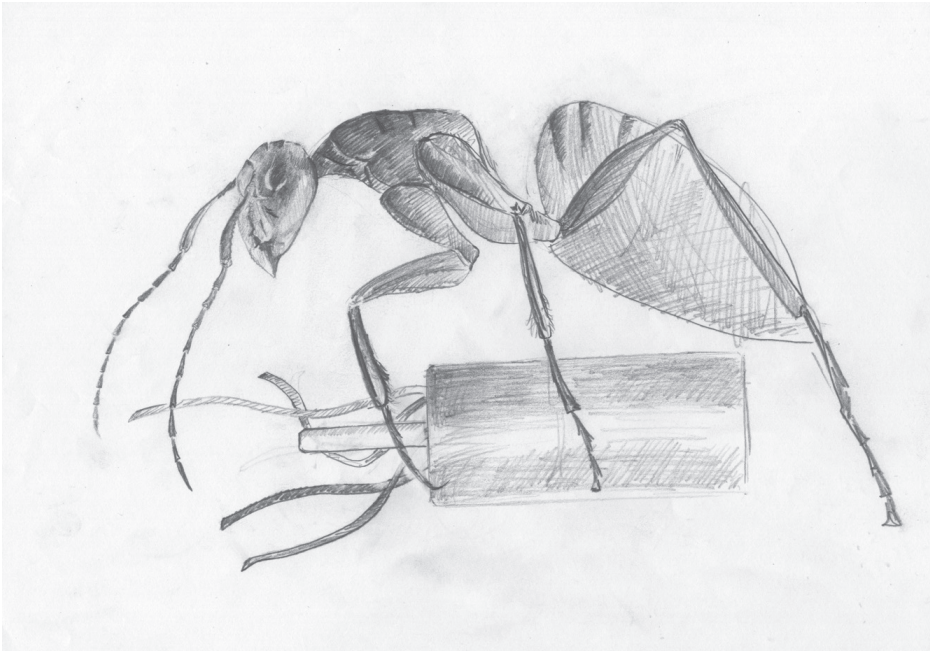
Abstract

In this study, we demonstrate the design, fabrication and characterization of a synchronous micro motor. The micro motor consists of flex print coils and a permanent magnet rotor. The size of the motor is 2.0 mm length and 1.0 mm outer diameter. With 1.0 A effective driving current, the motor can rotate a 0.3 mm mirror at a maximum speed of 3640 revolutions per second. The uniformity and accuracy of the motor was characterized at 50 Hz, 200 Hz and 3200 Hz driving frequencies. The performance improved by increasing the driving frequency, which was represented as better speed uniformity and lower angular error. The torque of the motor was estimated to be 0.25 to 0.27 μNm with 1.0 A current by fitting the measured speed based on the equation of motion. We describe the application of the micro motor as a distal actuator for intravascular imaging. We constructed optical and ultrasonic imaging catheters and show the intravascular images of coronary arteries obtained with these catheters.

2.1 | Introduction

Continuing miniaturization of mechanical systems, for instance in healthcare, has fostered a need for micro motors to actuate components. For minimally invasive medical applications, it is desirable to have an outer diameter of the instrument in the order of 1 mm. Various micro motors were developed over the past decades, driven by piezoelectric actuators or micro-electromechanical systems[41-44]. Although successful for a number of applications, the motors based on these working principles are limited to relatively low speeds of 10-50 revolutions per second (RPS). Instruments that require fast rotation (100-1000 RPS) cannot be realized based on these designs.

The synchronous motor is one of the most widely used types of alternating current (AC) motors. It has a relatively simple structure consisting of two basic components: a stator and a rotor. In either of the two, time-varying magnetic field is induced, which results in the rotation. Compared to other types of motors, one of the major advantages of synchronous motor is that the speed remains constant irrespective of the loads: the rotation is synchronous to the frequency of the driving current. Therefore, the synchronous micro motor is the preferable type of actuator where precisely constant speed is a critical requirement. One of these applications is minimally invasive imaging catheters. Catheters with a distal scanning mechanism show more uniform rotation, better tracking and control in mechanically challenging geometries, compared to devices which use a proximal motor and a flexible drive shaft[44,45]. The scanning of the image beam in such catheters is realized by rotating a small mirror by a micro actuator at the catheter tip. This application requires a micro actuator that can generate constant high speed at low driving power.

In this paper we describe a synchronous micro motor, rotating at constant high speed. By using a flexible print coil design, and a permanent magnet rotor, the motor can generate several thousands RPS speed with a relatively low current requirement. The size is 1.0 mm outer diameter (OD) and 2.0 mm length. We present the design in detail, and evaluate the performance of the motor in terms of maximum speed and rotation uniformity. We examine the magnetic field produced inside the motor by a finite element simulation. The maximum torque, damping, and friction in the motor are derived from an analysis of the equation of motion of the rotor.

2. 2 | Structure and working principle

The micro motor in our study is a two-phase, four-pole synchronous motor with a two-pole permanent magnet rotor. The stator consists of single-strand coils, realized in copper on flexible printed circuit. The magnet on the rotor (Sm_2Co_{17}) has a center bore containing a stainless steel shaft. Two ruby bearings were used to hold the rotor shaft inside a non-magnetic cylindrical housing (stainless steel). The front ruby bearing has four holes on its perimeter to allow the leads connecting to the coils to enter. The components of the micro motor are shown in Figure 2.1 (a)[46].

The stator coils were made out of copper (thickness 17 μm) on Kapton flexible print (thickness 25 μm). The flex print is rolled up inside the stainless steel housing, so the two coil pairs are diametrically opposite inside the motor. Furthermore, each coil has one main leg and two side legs as shown in Figure 2.2. By setting the width of the side legs as 71% of the middle leg width, the resistance in main leg was tuned to $\sqrt{2}/2$ times as that in each side leg. With this design, each coil produces a current density that approximates a sinusoidal distribution upon $\pi/4$ - $3\pi/4$ and $5\pi/4$ - $7\pi/4$ (see Figure 2.2). The coils are connected by a bottom strip on the print, which closes the circuit.

By running two sinusoidal current signals, with a $\pi/2$ phase shift, separately to the two coil pairs, a rotating magnetic field is produced which is approximately uniform inside the motor. A uniform magnetic field requires a sinusoidal distribution of the current density upon $0 - 2\pi$, which cannot be realized in the present design. Note that the magnetic field produced by the stator is directed along the circumference of the motor, rather than perpendicular like in traditional coil configurations. Figure 2.2 shows the mechanical effect of the configuration of the coils affecting the current density. The effective current density from the three legs of each coil is represented by rectangles.

The motor is fabricated by Kinetron B.V. Tilburg, the Netherlands according to the following procedure, illustrated in Figure 2.1: copper coils are attached upon a thin flexible circuit film and etched to the appropriate size and shape. By rolling up the circuit film, the coils form a tube with an outer diameter of 0.90 mm. The rolled-up coils are welded to four copper leads and inserted into the stainless steel tube that is the housing. A ruby bearing is inserted into the bottom of the housing. The permanent magnet is glued on the shaft to form the rotor, which is then inserted into the housing. The front ruby bearing, which has holes on its edge for the leads, is put in position to hold the rotor. In the final step, the contact parts of the shaft and the bearings are lubricated to decrease the frictional resistance. The mechanical schematic design is shown in Figure 2.1(b). The final dimension of the motor is 2.0 mm length and 1.0 mm OD. The photograph of the micro motor next to a coin of 10 Euro cents is shown in Figure 2.1 (c).

To drive the motor, the sinusoidal current signals, offset by a $\pi/2$ phase difference, were programmed with an arbitrary waveform generator. The two driving signals were amplified by a balanced current amplifier to ensure the sinusoidal shape of the current[33]. Since the rotor moves synchronous to the rotating magnetic field, the rotating speed (in RPS) equals the frequency (in Hz) of the driving signal. Therefore, quantitative control of the rotating speed can be realized by setting the frequency of the driving current. The motor typically requires a drive current up to approximately 1 A, depending on the desired speed. The impedance of the motor is mainly determined by ohmic resistance of the coils and equals approximately 0.30 Ω.
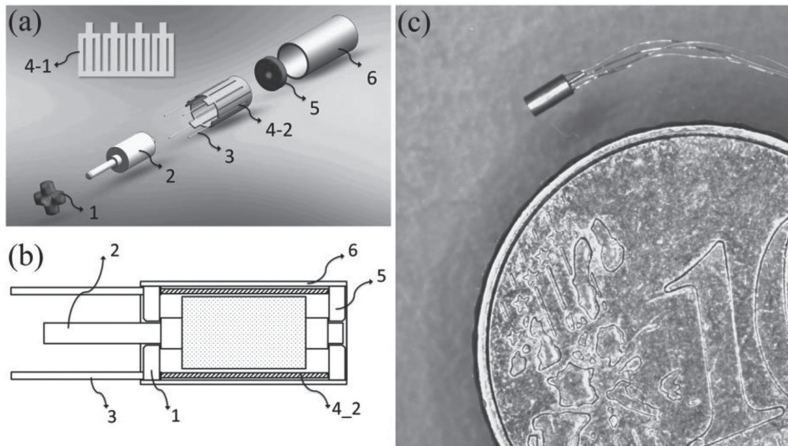
Figure 2.1 | (**a**) Components of the micro motor: 1) Upper ruby bearing; 2) Permanent rotor (Sm2Co17); 3) leads (copper); 4-1) flexible print coil before rolling (copper); 4-2) coil after rolling; 5) bottom ruby bearing; 6) stainless steel housing. (**b**) Mechanical schematic diagram of the synchronous motor, (**c**) Photograph of the motor next to a 10 Euro cent coin.
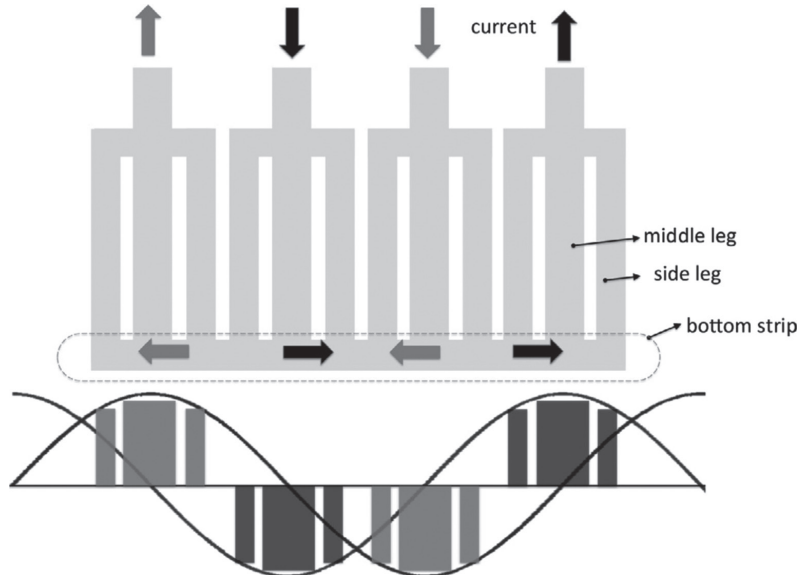
Figure 2.2 | Schematic of the coils design and the mechanical effect of the coils. The black current has $\pi/2$ phase delay to the gray current.

Based on the design of the motor, we built a finite element model (FEM) of the coils using ANSYS (ANSYS Maxwell student version, Pennsylvania, U.S.A.) software to simulate the magnetic field inside the motor. The analysis produced a rotating two-pole magnetic field generated by the coils, as designed. The magnetic field is largely uniform inside the coils as shown in Figure 2.3. In this simulation, we ignored the effect of the "bottom strips", connecting the main poles, that produce a field in the direction along the shaft.
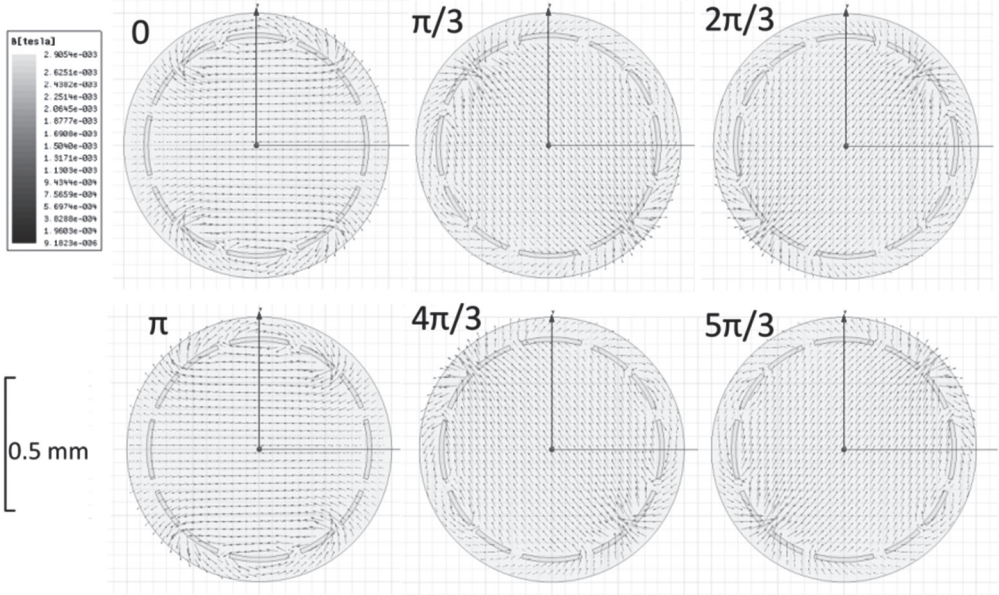
Figure 2.3 | Cross-sectional view of the magnetic field simulated based on FEM of the flexible print coils. The phases of the driving signal ranges from 0 to 5π/3 with a step of π/3. The driving current has 1A effective value.

2.3 | Speed characterization experiments

To quantitatively evaluate the rotation behavior of the driven motor, we built a setup to measure the instantaneous speed of the motor. The schematic diagram of the setup is shown in Figure 2.4(a). The motor is mounted vertically in the center of a black cylindrical-shape film, and there are 80 slits with 1.0 mm width on the film. On the shaft of the motor, a coated prism (leg dimension is 0.3 mm) was mounted. The prism deflects a 632 nm wavelength laser beam sideward to the film. When the prism is rotated by the motor, the deflected light beam scans the film horizontally. The laser beam that falls through the slits is detected by photo diodes. The central angle between two neighboring slits is 4.5°, and the first slit is blocked to indicate the start point of one rotating revolution. As shown in Figure 2.4(b), the digitized data of each rotating revolution consists of 79 peaks and a missing peak. The scanning time

between two slits can be read by measuring the corresponding time between two peaks. Based on the scanning time, average angle speed within the 4.5° can be calculated.
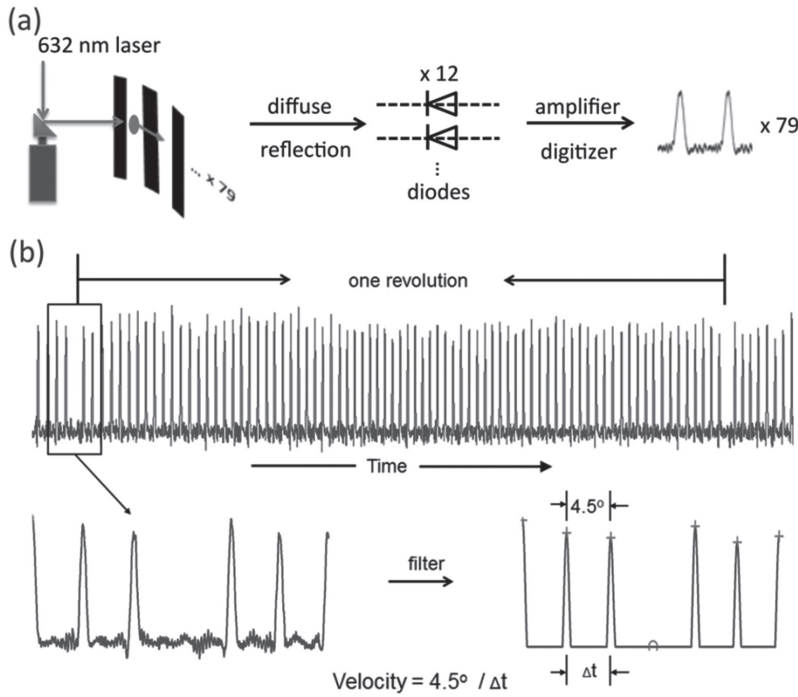
Figure 2.4 | (a) Schematic diagram of the speed measurement. **(b)** Schematic diagram of the digitized data of one rotating revolution identified by two missing peaks. The velocity is the average speed of each 4.5° angle.

2.3.1 | Maximum stable speed

To achieve a target rotating speed, the spinning up procedure is important. Any sudden relative displacement between the rotor and the coils may cause a strong oscillatory speed ripple, or even stop the motor. Therefore, we applied a driving signal with an increasing frequency. As an example, Figure 2.5(a) shows how the frequency reaches 3200 Hz in 3 seconds by sweeping up the frequency in a programmed gradient. We measured the maximum speed of the motor under different effective values of current. Figure 2.5(b) shows that the stable maximum speed increased with driving current. A maximum speed of 50 RPS (which would be typically needed for slow scanning applications such as intravascular ultrasound, IVUS) was reached with a current of 0.14A. A maximum speed of 3200 Hz, such as required for high-speed intravascular optical coherence tomography (IV-OCT), was achieved with a driving current of 0.9A effective value. At a current of 1.0 A, the temperature rise of the motor was

measured to be 4.7 K in air and 1.9 K in liquid environment after running for 7 seconds. At 0.14 A, no significant temperature rise of the motor was observed after running the motor for hours in air.
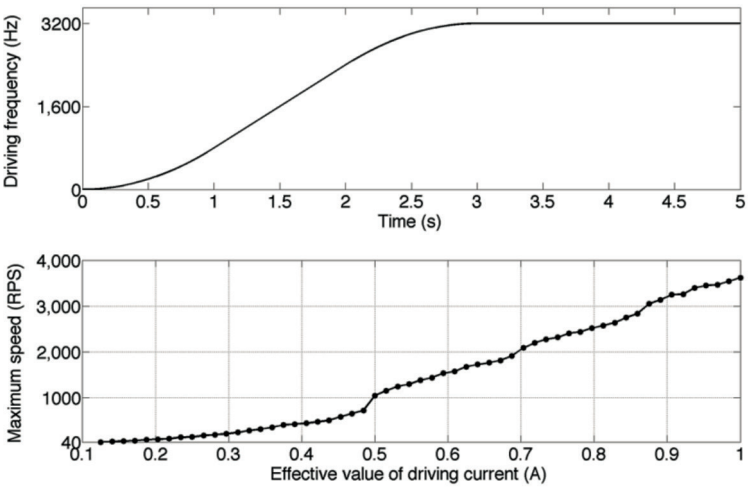
Figure 2.5 | (a) Plot of driving frequency versus time for 3200 RPS speed. (b) Maximum stable speed of the motor increases with the driving current.

2.3.2 | Speed uniformity

Besides the maximum speed, speed ripple is another important quantifier of motor performance. We evaluated the uniformity of the rotation velocity at 200 RPS, while changing the amplitude of the driving current. We calculated the relative standard deviation (SD) and the maximum relative speed error of the speed over 20 revolutions. As shown in Figure 2.6, in general, the relative SD and maximum relative speed error both increase with the current amplitude. Therefore, to have a uniform rotation, the motor should be applied with the lowest required current. We interpret this behavior as an increasing influence of the driving field heterogeneity at higher currents.

In the second step, we measured the speed uniformity upon 20 revolutions at 50 Hz, 200 Hz and 3,200 Hz at the lowest required driving current. As shown in Figure 2.7, the speed ripple is stronger at low speed than that of high speed. This is because at low speed the damping resistance (proportional to the velocity) is small. With such small damping resistance and relatively big driving torque, any variations in the speed will damp out slowly and give rise to oscillations during rotating at low speed[47]. The relative speed errors and the relative SD at different driving frequencies are shown in Table 2.1.
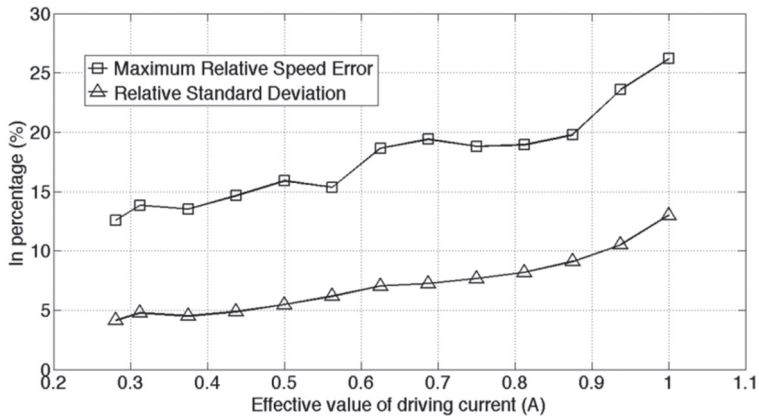
Figure 2.6 | Maximum relative speed error and relative standard deviation of the rotating speed increase with effective value of the driving current. The driving frequency was set to 200 Hz.
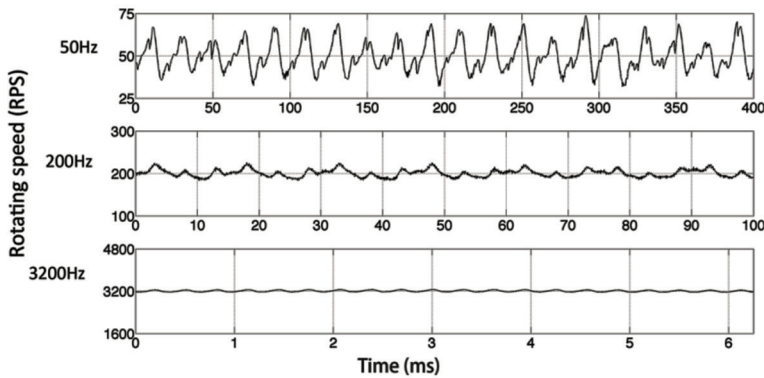
Figure 2.7 | Instantaneous speed of the motor driven at lowest required current with different driving frequencies as (**a**) 50 Hz (0.25 A), (**b**) 200 Hz (0.45 A) and (**c**) 3,200 Hz (0.90A).

2.3.3 | Position error

The position error is defined as the difference between the actual angular position and the expected angle (the ideal velocity multiplied by time). Position error represents how serious the non-uniform rotation will distort imaging (NURD). We calculated the actual position by integrating the instantaneous velocity over time. The position errors over 20 revolutions at 50 Hz, 200 Hz and 3200 Hz are shown in Figure 2.8. As a consequence of the spinning-top effect, the position error is much larger at low speed than at high speed. At 50 Hz (for IVUS imaging), the SD of position error is 10.1° with a maximum error of 24.2°. Thus a relative stronger NURD is expected in IVUS imaging. However, when the frequency reaches 3200 Hz, the error is less than 5.0° with a SD of 2.7°. In this situation, the NURD influence in OCT

images will be much smaller than that in IVUS. A slower sine wave ripple (period: approximately 6.3 ms) is observed at 3200 Hz, which may be due to lengthwise movement of the shaft. The position errors at different driving frequencies are also listed in Table 2.1.
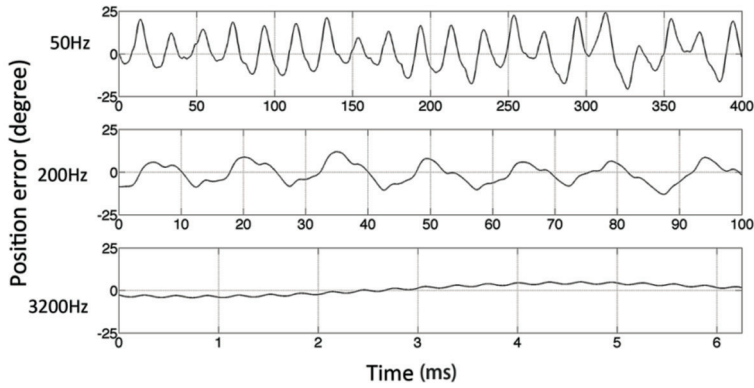
Figure 2.8 | Position errors versus time at different driving frequencies.

Table 2.1 | Speed uniformity and position error of the motor driven at different frequencies.

Driving frequency	Relative SD of speed (%)	Maximum Relative speed error (%)	SD of angular error (degree)	Maximum angular error (degree)
50 Hz	8.2	17.9	10.1	24.2
200 Hz	4.1	12.6	5.2	13.1
3200 Hz	0.9	1.7	2.7	5.0

SD: standard deviation

2.3.4 | Damping coefficient and torque estimation

The maximum driving torque is an important parameter for a synchronous motor. Due to the small size of the motor, direct measurement of the driving torque is difficult. As an alternative, we estimate the dynamic parameters of the motor by analyzing its response to a step impulse and fitting the measurement with a model based on a second order differential equation describing the rotor. In general, the driving torque depends on the current and the angle between the rotor and the stator field[48,49]. The torque generated by the two coil pairs follows this equation:

$$\tau_1 = -A_1 \cdot I_1 \cdot sin(\alpha) - A_2 \cdot I_2 \cdot cos(\alpha) \tag{1}$$

τ_1 is the driving torque, A_1 and A_2 are constants linking the generated torque to the driving currents, I_1 and I_2 are the instantaneous currents in coil pair 1 and coil pair 2 separately, α is the angle lag of the rotor to the magnetic field of coil pair 1. We assumed that the viscous resistance of the air and

lubricant inside the motor are the main contributors to the damping since the air-drag of the tiny prism (0.3mm) is relatively small. Therefore the damping coefficient is proportional to the rotating speed. The dynamic friction torque τ_f can be considered constant during rotation (and zero otherwise). Therefore, the motion equation of the rotor is as follows[50,51]:

$$\tau_I = -A_1 \cdot I_1 \cdot sin(\alpha) - A_2 \cdot I_2 \cdot cos(\alpha) = M \cdot \ddot{\alpha} + \tau_f + k \cdot \dot{\alpha} \tag{2}$$

M is the inertia moment, τ_f is the resistance torque (depending on the loading of the motor and friction) and k is the damping coefficient. Since an analytic solution for the second order differential equation, resulting from insertion of (1) in (2), is not achievable, we used Matlab/Simulink to estimate the parameters of the equation based on our measured speed data[52]. We applied a torque impulse by setting the rotor to α = -90° manually, and then supplying coil pair 1 with a single-channel direct current (DC) signal (1.0 A). The speed was recorded when the motor moved to its new equilibrium position from -90°. By using least squares minimization, three parameters were estimated (τ_f, k and A_1). The experiment was repeated by supplying DC signal to coil pair 2 only to estimate A_2. The Simulink model for the motion equation is shown in Figure 2.9(a); the speed recording, compared to the estimated fitting curve is shown in Figure 2.9(b). The estimated parameters, based on 6 measurements for each coil pair, are listed in Table 2.2. M was not measured but calculated using the known dimensions and material densities of the rotor.
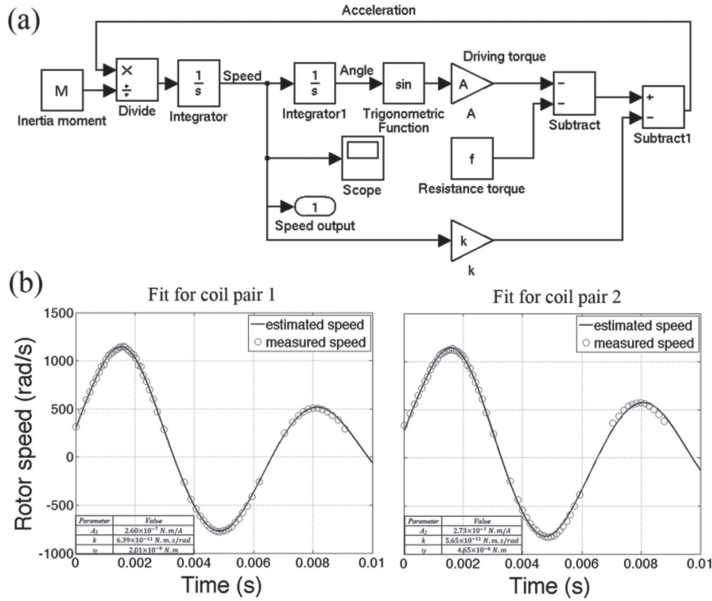
Figure 2.9 | (a) Simulink model for the motion equation and the estimated parameters τ_f: Resistance torque, k: Damping coefficient, M: Inertia moment, A_1 and A_2: Constant value. (b) The estimated speed comparing with measured speed. The original angle of the rotor was set to -90°; and the stator magnetic field was 0° by applying 1.0 A constant current to one coil pair.

Table 2.2 | Estimated parameters of the micro motor.

| Parameter	Value	Unit
A_1	2.55±0.09	$10^{-7}\ N.m/A$
A_2	2.61±0.13	$10^{-7}\ N.m/A$
τ_f	2.99±2.08	$10^{-8}\ N.m$
k	9.24±3.74	$10^{-11}\ N.m.s/rad$
M	2.61	$10^{-13}\ kg.m^2$

2. 4 | Minimally invasive imaging application

2.4.1 | IV-OCT imaging

Having characterized the micro motor, we built a catheter for intravascular imaging using OCT[53]. In the catheter, far-infrared laser beam (1310 nm central wavelength) was focused by a gradient refractive index (GRIN) lens and deflected sideward by a mirror mounted on the rotor. The dimension of the catheter is 1.3 m length and 1.1 mm OD at the tip. The schematic diagram and the photograph of the catheter, a photograph of the catheter tip, and the motor are shown in Figures 2.10(a-c). Speed is a concern in IV-OCT, hence fast rotation of the imaging beam is desirable. The high-speed rotation of the motor allows us to acquire up to 3200 frames per second (FPS). The catheter is mounted on a programmable linear stage to pull it back inside the artery under investigation. With a pullback speed of 100 mm/s, the data acquisition of the entire artery was finished in < 1 s. *Ex vivo* cross-sectional images of human artery are shown in Figure 2.10 (d) and (e). An imaging speed of 400 FPS provides a frame pitch of 250μm, which is close to the current commercial IV-OCT systems. On the other hand, 3200 RPS rotating speed reduces the frame pitch to 31μm. The eightfold difference in frame pitch has a clear impact on the longitudinal image quality (a cross section through the data set in a plane containing the catheter) as shown in Figure 2.10 (f) and (g). Four show areas (at 2, 4, 8 and 11 o'clock) in Figure 2.10 (d) and (e) were caused by the four leads of the micro motor.

2.4.2 | IVUS imaging

The initial development of the micro motor[46] was driven by IVUS imaging. An IVUS catheter was built based on the motor and applied *in vivo*[45]. Limited by the data acquisition speed of IVUS system, the scanning speed of the motor was set to 50 RPS. IVUS requires a fluid-filled catheter, and a larger mirror. Both contributed to a reduction of the speed ripple at this relatively low rotation velocity. The ultrasonic transducer (30 MHz frequency) was mounted on the tip of the catheter. The dimension of the catheter was 1.3 m length and 1.3 mm OD. The schematic diagram and the photograph of the IVUS catheter are shown in Figure 2.11(a) and (b). Since the shaft of the motor (front side) is facing the catheter tip, the motor leads were connected at the back side of the motor. The photograph of the micro motor for IVUS is shown in Figure 2.11(c). Figure 2.11 (d)-(f) shows the IVUS images of different tissue types that were acquired with the catheter.
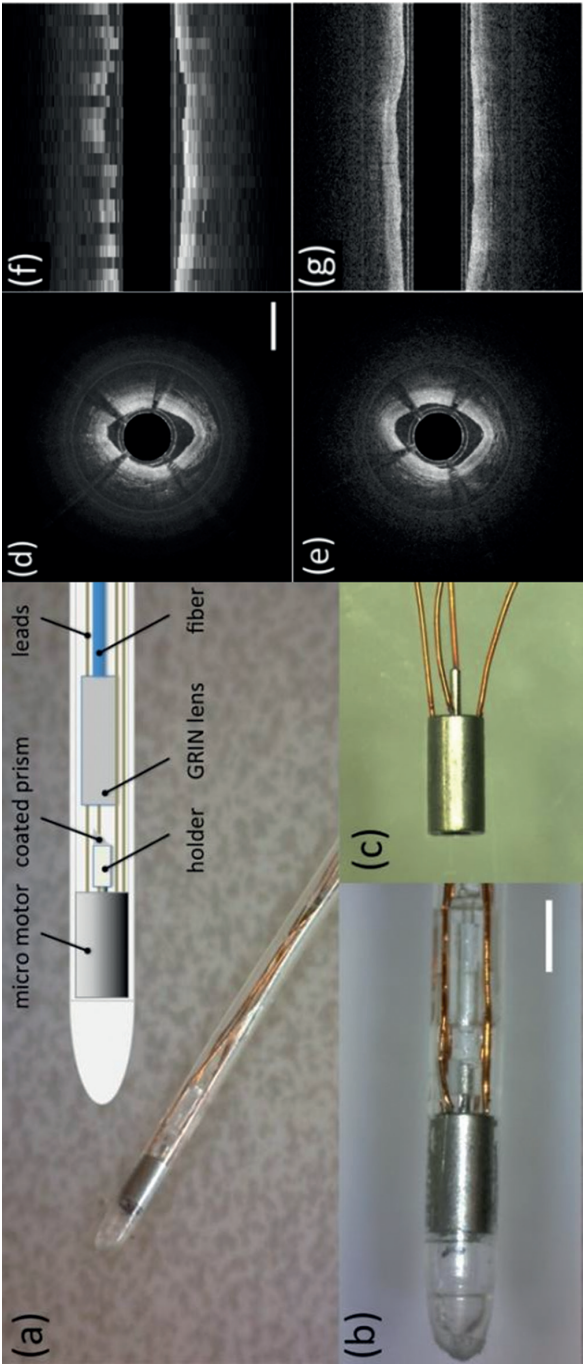
Figure 2.10 | (a) Schematic and photograph of micro-motor based OCT catheter. (b) Photograph of micro-motor based OCT catheter. (b) Photograph of IV-OCT catheter tip. (c) Photograph of the micro motor. (d) Cross-sectional image of human artery acquired at 400 REV/S scanning speed. (e) Cross-sectional image of human artery acquired at 3200 REV/S. (f) Longitudinal image of the artery acquired at 400 REV/S. (g) Longitudinal image of the human artery acquired at 3200 REV/S. The length of the scale bar in (b) and (d) is 1.0 mm.

2
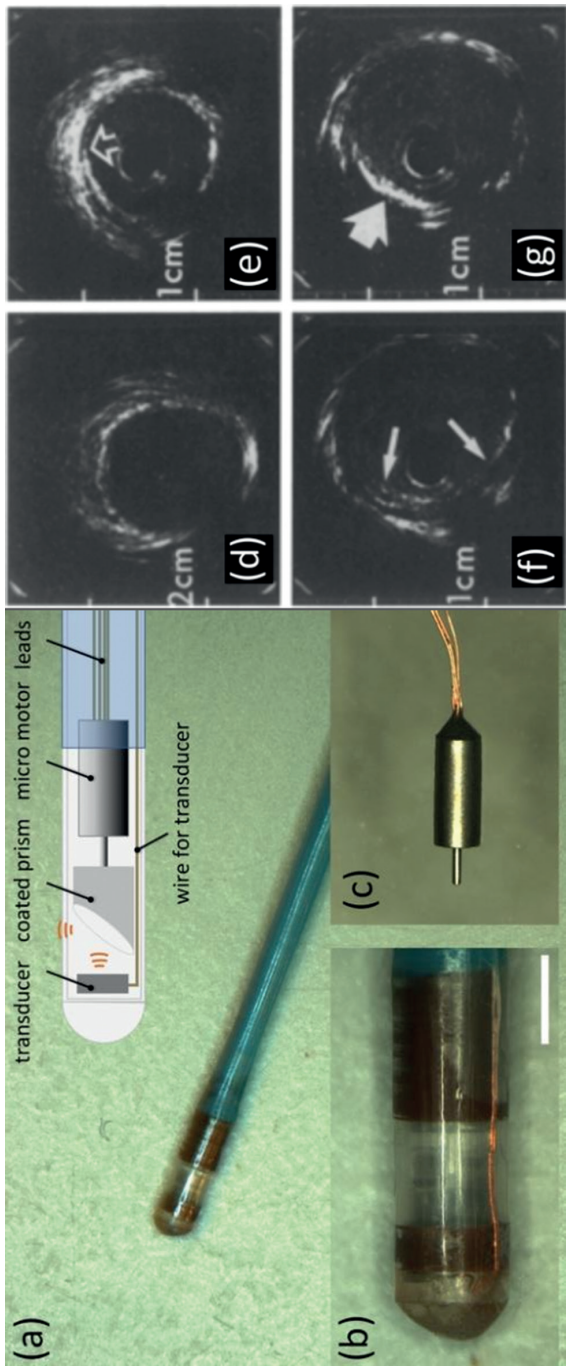
Figure 2.11 | (a) Schematic and photograph of micro motor based IVUS catheter. (b) Photograph of IVUS catheter. (c) Photograph of IVUS catheter tip. Scale bar is 1.0 mm. (c) The micro motor used in the catheter, which has the leads opposite direction from the shaft. (d) IVUS image of normal segment. (e) Segment with intimal thickening indicated by an open arrow. (f) Eccentric plaque formation indicated with solid arrows. (g) Segment with calcium deposits indicated with solid arrow. (d)-(g) from [5].

2.5 | Discussion

We presented a description and characterization of a permanent magnet synchronous micro motor, with stator coils printed on a flexible circuit. We measured the motor speed as a function of drive current, studied the uniformity of the rotation, and evaluated the maximum torque. Finally we discussed application of the device in catheter-based imaging.

A current-driven motor in a confined geometry can generate a temperature rise due to resistive heating. Even though we envision this motor to be applied in vascular imaging, where the blood provides cooling, it is worthwhile to consider the maximum temperature rise that can be generated during motor operation. At 50 Hz and 0.14 A, the motor radiates all its heat effectively and the temperature remains stable for hours. However, Running the motor at 1.0 A for 7 seconds will cause a 4.7 K temperature rise. Running the motor at high driving current for a long time may damage the motor, for instance by melting of the solder joints of the leads to the coils. Nevertheless, for the high-speed intravascular application (0.9A-1.0A), 7 seconds is much longer than necessary and the temperature rise is less than 1.9 K when taking liquid flush into account. Such a temperature rise (4.7 K in air, 1.9 K in liquid) is comparable to the change brought about by a metal coronary stent in an clinical Magnetic Resonance Imaging scans, which is deemed acceptable [44] . In this situation, we believe that the temperature rise as a result of operation at a drive current of 0.9-1.0A will not be a critical problem for in-vivo imaging application.

For application in IV-OCT imaging, the issue of shadows, caused by the motor leads, presents. Each shadow area covers approximately 2.5% area of the image. Though 2.5% area can be ignored for plaque imaging, it is large enough to block a stent cell for stents evaluation. To solve this issue, twisted thinner leads can be used to reduce the four shadow areas into one. This will require a larger diameter of the catheter and the heating issue needs to be re-evaluated.

The coils were designed to approximate a uniform magnetic field inside the motor. In principle, at least two magnetic field components (in x and y-axis) need to be generated separately to perform a rotating magnetic field. Each magnetic field component needs a pair of coils. Though using more coil pairs can give a more uniform magnetic field, it will also introduce more difficulties in manufacturing and require more leads that will cause shadow areas in the IV-OCT image.

Two issues are still affecting the magnetic field, and may contribute to the speed ripple we observed. The first is the magnetic field generated by the bottom strip connecting the coils. This part of the coil construction carries a current that is directed along the shaft. We presently neglect this contribution, as it is perpendicular to the rotor magnetic field and relatively far away from the rotor. The second issue is the missing magnetic field due to the coil distribution upon $\pi/4$ - $3\pi/4$ rather than $0 - \pi$, which leads to readily apparent curvature of the field in the FEM simulation. These two issues may further strengthen the speed ripple during rotating. To better understand these issues, an experimental study or an ANSYS

simulation study of these magnetic field errors can be helpful to optimize the coil design and minimize their influence. This is the subject of further development.

Previous studies have demonstrated several micro actuators for minimally invasive imaging applications. For instance, a three-phase, brushless motor (2.0 mm OD, 6.0 mm length) capable of 1200 RPS was recently developed for endoscopic catheter[54]. Another novel hollow ultrasonic motor was demonstrated[44]. With a size of 1.0 mm OD and 5.6 mm length, the motor can rotate at 33 revolutions per second (RPS) under 7V driving voltage. Limited by the dimension requirement, these actuators are not suitable for intravascular imaging[55].

2.6 | Conclusion

In summary, we demonstrate a synchronous micro motor consisting of a permanent rotor and a flexible coil. This motor enables high-speed rotation with a very small outer diameter. Within a size of 1.0 mm OD and 2.0 mm length, the micro motor can rotate a micro prism at 3620 RPS with a driving current of 1.0 A. The micro motor can also rotate the prism at lower speed with a lower current. We found that the rotation at high speed was uniform to within 2%, and increased for lower speed and with increasing the drive current above the minimum required for stable rotation. We estimated the torque indexes of both coil pairs by fitting the measured speed based on the motion equation. The results showed that the motor could generate a torque approximately from 0.25 to 0.27 μNm with 1.0 A current. By using our micro motor as the distal actuator in intravascular catheters, IV-OCT images and IVUS images were acquired *in vitro* and *in vivo* separately. The acquired images show that the motor rotation during pullback is not affected by passage through tight sections with hard (calcified) tissue. We believe that the micro motor has many other potential applications due to its rotating performance and low current requirement.

Acknowledgements

Chapter 3

Intravascular optical coherence tomography imaging at 3200 frames per second

Tianshi Wang, Wolfgang Wieser, Geert Springeling, Robert Beurskens, Charles T. Lancee, Tom Pfeiffer, Antonius F. W. van der Steen, Robert Huber, and Gijs van Soest

Abstract

We demonstrate intravascular optical coherence tomography (OCT) imaging with frame rate up to 3.2 kHz (192,000 rpm scanning). This was achieved by using a custom-built catheter in which the circumferential scanning was actuated by a 1.0 mm diameter synchronous motor. The OCT system, with an imaging depth of 3.7 mm (in air), is based on a Fourier domain mode locked laser operating at an A-line rate of 1.6 MHz. The diameter of the catheter is 1.1 mm at the tip. Ex vivo images of human coronary artery (78.4 mm length) were acquired at a pullback speed of 100 mm∕s. True 3D volumetric imaging of the entire artery, with dense and isotropic sampling in all dimensions, was performed in < 1 second acquisition time.

3.1 | Introduction

Optical coherence tomography (OCT) can perform high-resolution, cross-sectional imaging of biological tissue[45]. Since its introduction into the field of cardiology, OCT has become a valuable tool for diagnostic plaque imaging and intervention guidance[56,23]. In current intracoronary OCT catheters, the side-view scanning is realized by rotating the entire optical fiber in the catheter with a proximal motor. A lens/mirror assembly at the fiber tip directs the beam sideways toward the artery wall. The rotating catheter is pulled back inside the lumen of the artery under investigation to acquire a volumetric dataset[20,23].

The fastest commercial intravascular OCT systems acquire 160 frames/second with 500 lines/frame, and the pullback speed is limited to 40 mm/s[57]. In this situation, the images are undersampled in the pullback direction: Only 12% of the lumen is sampled because the sampling interval of 250 μm is much larger than the transverse resolution, which is approximately 30 μm. In clinical situations, the cardiac motion also affects the OCT acquisition. The pullback procedure for the whole artery takes several seconds. The cardiac motion during acquisition will cause inaccuracy in frame spacing and possibly frame order, due to motion of the catheter along the vessel. This can affect the fidelity of the longitudinal rendering and 3D visualization of the data. We propose to solve these issues by further increasing the speed of intravascular OCT.

In this Letter, we describe an ultrafast intravascular OCT system consisting of a micromotor-based catheter and a dispersion compensated Fourier domain mode locked (FDML) laser, operated at 1.6 MHz depth scan rate[58-60]. The system improves the image quality in longitudinal direction and shows the potential to acquire OCT data of a complete coronary artery within one cardiac cycle.

3.2 | Methods

The high frame rate catheter we developed is based on a customized two-phase synchronous micromotor[46,61] (Kinetron BV, The Netherlands). The small size [1.0 mm outer diameter (OD), 2.0 mm length] of the motor allows mounting into the catheter tip. Four copper wires (70 μm OD) were soldered to the motor to provide the drive signal. A coated prism (Edmund Optics, NT66-770) was attached to the motor shaft by a plastic holder. The motor was mounted into a 1.1 mm OD transparent polyethylene terephthalate (PET) tube to form the catheter tip. A 1.3 m length optical fiber (SMF28) with a gradient refractive index (GRIN) lens (Agiltron, USA) on the tip was used to transmit and focus the light beam. The catheter body, consisting of current leads, fiber, and protective tube [1.25 m length polyethylene (PE)], was thermally welded to the tip to create a sealed device. The final size of the catheter is 1.3 m length and 1.1 mm OD at the tip. The imaging beam forms a 20 μm beam waist at 1.6 mm working distance in air. The catheter tip and schematic drawing of the catheter are shown in Figure 3.1(a) and 1(b).

To drive the catheter, two-phase sinusoidal current waveforms need to be supplied to the two frame coils inside the motor. The speed of the motor is controlled by the frequency of the drive currents, and is stable to within 2%. The drive signals were programmed using an arbitrary waveform generator (AWG; Agilent 33522A) and amplified to around 1.0 A (effective value) by a custom-built balanced current amplifier. The maximum speed of the micromotor we achieved is 3.5 kHz (210,000 rpm), reached by linearly increasing the drive frequency from 0.1 to 3.5 kHz within 0.2 s.

An imaging system was built based on a 1310 nm center wavelength, 1.6 MHz sweep rate (402 kHz, 4x buffered) FDML laser with dispersion compensation[60]. The 90 nm sweep range provided a resolution of 12 μm in tissue and a usable imaging depth of up to 3.7 mm (in air). The interferometer made use of a 1.0 GHz balanced photo receiver (Wieserlabs, WL-BPD1GA) and a 1.5 GS/s 8 bit data acquisition board (Signatec, PX1500-4). The motor drive signal generated by the AWG was also used as the acquisition trigger signal. A sensitivity of 102 dB was measured with 53.5 mW power on the sample, which is close to shot noise limit of 103 dB. The high-speed pullback was performed by a programmable linear motor stage (Aerotech, ACT115DL) with 200 mm long rail and up to 30 m/s² acceleration. The schematic of the system is shown in Figure 3.1(c).

3.3 | Results

Ex vivo imaging experiments were carried out with a human left anterior descending coronary artery (LAD, female aged 71) in phosphate buffered saline. The artery was obtained from Department of Pathology of the Erasmus University Medical Center, in accordance with a protocol sanctioned by the local ethics committee. The catheter was inserted into the artery manually and pulled back by the linear motor stage. In order to ensure a stable rotation speed during pullback, the rotation speed was reduced to 3.2 kHz (192,000 rpm). 3D datasets at 400 Hz and 3.2 kHz frame rate were acquired separately. The 3D dataset of the entire LAD artery (2-4 mm lumen, 78.4 mm length) was acquired by pulling back the catheter at 100 mm/s.

The cross-sectional images acquired at 400 Hz consist of 4010 lines, densely sampling the image. The trigger rearm time causes six lines per frame to be dropped. As shown in Figure 3.2(a), adjacent lines were averaged to 1002 lines in groups of four to gain a slightly higher dynamic range. Figure 3.2(b) shows the cross sectional image acquired at 3.2 kHz frame rate consisting of 496 lines. Calcified plaque was observed in the area from 4 to 7 o'clock in the image. An impurity inside the PET tube caused a reflection, visible at 4 o'clock. The shadows of four copper wires were also observed at 1, 3, 6, and 9 o'clock. The 3D reconstruction based on 3.2 kHz frame rate is shown in Figure 3.2(c). Post-processing took several minutes on a 2.5 GHz Macbook Pro. A video recording of the calcified plaque at 3.2 kHz is available online.
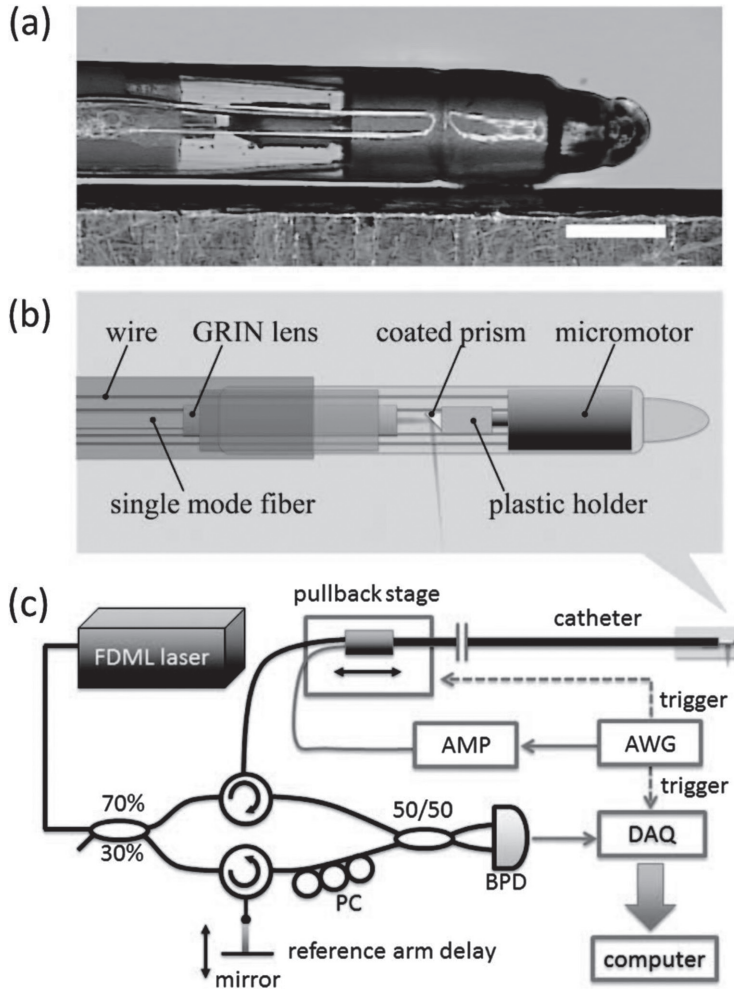
Figure 3.1 | (**a**) Photograph of the catheter tip. The scale bar presents 1.0 mm. (**b**) Detailed schematic drawing of the catheter. The OD of the catheter is 1.1 mm at the tip. GRIN lens, Gradient index lens. (**c**) Diagram of the experiment setup (optics, black; electronics, gray). AMP, current amplifier; AWG, arbitrary waveform generator; BPD, balanced photodiodes; DAQ, data acquisition; PC, polarization controller.
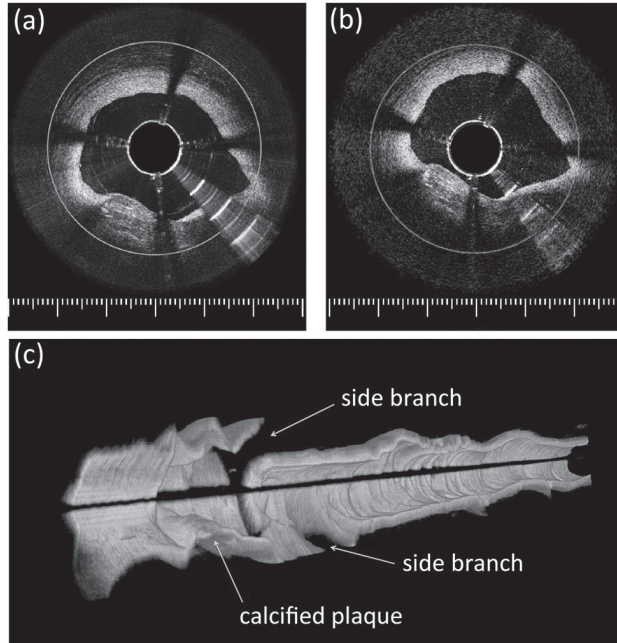
Figure 3.2 | Cross sectional images of human coronary artery at (**a**) 400 Hz (1002 lines averaged from 4010 lines), (**b**) 3.2 kHz (496 lines) frame rate, and (**c**) 3D reconstruction of the artery cut along the vertical plane. In (**a**) and (**b**), calcified plaque was observed at 4 to 7 o'clock, which was also illustrated in (**c**). The reflection at 4 o'clock was caused by an impurity. The ring artifacts at approximately 2 mm were caused by the internal reflection on the interface between GRIN lens and fiber. The rulers in (**a**) and (**b**) represent 6.0 mm.

At 400 Hz frame rate and 100 mm∕s pullback speed, the sampling interval in longitudinal direction is 250 μm, which is comparable to the frame pitch offered on current commercial scanners. At 3.2 kHz frame rate, the line density in cross sectional images of about 500 lines per frame is similar to conventional intravascular OCT systems. However, the sampling interval in the longitudinal direction is reduced to 31 μm, similar to the transverse resolution. The longitudinal sections through the pullback data sets at different frame rates are displayed in Figure 3.3. The eightfold difference in sampling interval has a clear impact on the level of anatomic detail that can be seen.
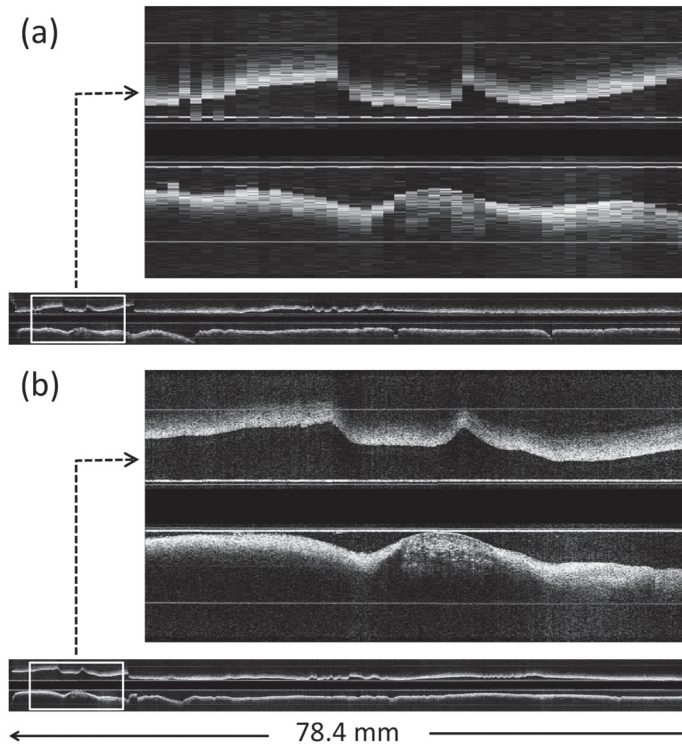
Figure 3.3 | Advantage of high frame rate: Longitudinal images of coronary artery (78.4 mm) at (**a**) 400 Hz frame rate and (**b**) 3.2 kHz frame rate. The A-line rate was 1.6 MHz. The magnified parts in (**a**) and (**b**) display the same calcified plaque as in Figure 3.2. The pullback speed was 100 mm/s. The arrow shows the pullback direction.

3.4 | Discussion

In summary, we performed ultrafast intravascular OCT imaging of a human coronary artery. The OCT system relies upon a combination of a fast micromotor, capable of multi-kHz rotation speed, and a fast laser, capable of MHz sweep rate. Previous studies have explored the advantages of micromotor-based catheters[62-64]. A size of 1.65 mm OD was demonstrated, reaching a maximum frame rate of 200 Hz[64], similar to cable-driven rotating catheters. FDML lasers have been applied to endoscopic imaging at lower speed[65,66], but MHz FDML OCT has only been demonstrated for retinal imaging in ophthalmic application and for imaging in a bulk microscopy setup[60].

Two factors need to be optimized before applying the system to *in vivo* imaging. First, to meet the geometry requirement of the artery, the rigid part of the catheter needs to be shortened to about 5 mm (approximately 10 mm currently). This can be realized by replacing the GRIN lens by a ball lens, direct mounting of the reflector on the motor axle, and elimination of the stiff weld at the PE/PET

tube junction. Second, further miniaturization of the device should allow the fitting of an outer tube to contain the catheter body.

3.5 | Conclusion

The ultrafast intravascular OCT scanner we demonstrate in this study allows the acquisition of a fully sampled 3D data set of a coronary artery in less than a second. The shorter procedure will eliminate cardiac motion artifacts and further reduce the amount of flush media needed for imaging. It also significantly improves the longitudinal rendering of the pullback, a display mode that is widely used in clinical practice.

Acknowledgments

Chapter 4

Heartbeat optical coherence tomography: motion-free three-dimensional *in vivo* coronary artery microscopy

Tianshi Wang, Tom Pfeiffer, Evelyn Regar, Wolfgang Wieser,
Heleen van Beusekom, Charles T. Lancee, Geert Springeling, Ilona Krabbendam,
Antonius F.W. van der Steen, Robert Huber and Gijs van Soest
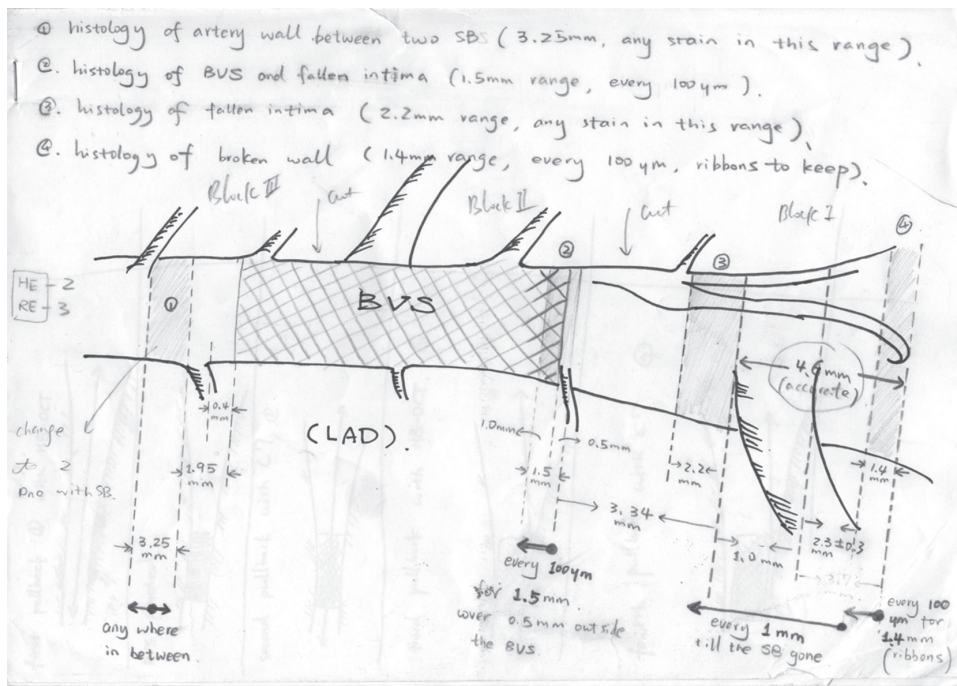
Chapter 5

Numerical analysis of astigmatism correction in gradient refractive index lens based optical coherence tomography catheters

Tianshi Wang, Antonius F. W. van der Steen and Gijs van Soest
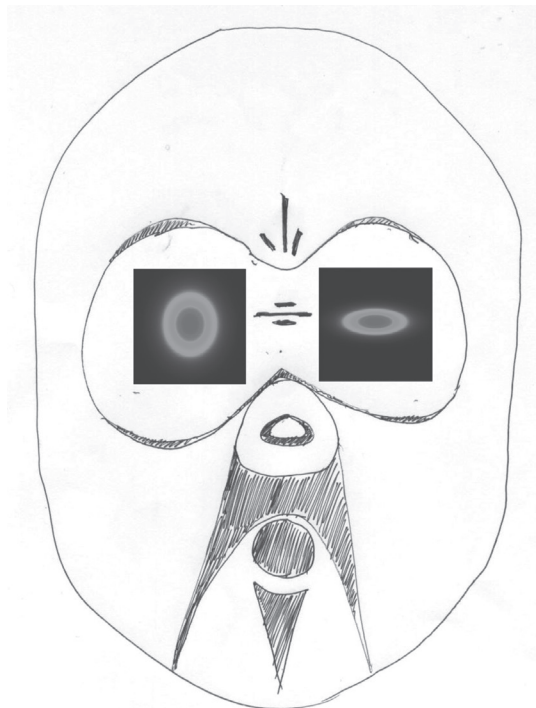
Abstract

Endoscopic optical coherence tomography (OCT) catheters comprise a transparent tube to separate the imaging instrument from tissues. This tube acts as a cylindrical lens, introducing astigmatism into the beam. In this report, we quantified this negative effect using optical simulations of OCT catheter devices, and discuss possible compensation strategies. For esophageal imaging, the astigmatism is aggravated by the long working distance. For intracoronary imaging, the beam quality is degraded due to the liquid imaging environment. A nearly circular beam profile can be achieved by a curved focusing optics. We also consider the method of matching refractive indices, and it is shown to successfully restore a round beam.

5.1 | Introduction

5.1.1 | Background
Optical coherence tomography (OCT) can perform non-invasive, cross-sectional imaging of biological tissue[8]. OCT is widely used in biomedical analysis and medical diagnosis, offering high-resolution (approximately 15 μm) imaging of tissue, with an image penetration depth of 1-2 mm, depending on tissue optical properties. It is commonly applied in ophthalmology for diagnosis of retinal diseases[81] and increasingly for endoscopic applications as well[69].

In endoscopic OCT for both coronary and esophageal imaging, the established methods use a guidewire or an endoscope instrumentation port to direct a catheter along into the lumen of the organ under investigation. When the catheter is positioned at the region of interest, cross-sectional images are acquired by rotary side-view scanning[82-86]. The side-view scanning can be realized by rotating the optical tip of catheter with a proximal motor. The rotating imaging element is pulled back inside the lumen under investigation to acquire a volume data set.

Two important applications of endoscopic OCT are imaging of the coronary circulation and of the upper gastrointestinal tract. Studies have shown the capability of OCT to perform screening for Barrett's esophagus, delineating gastrointestinal mucosal microstructure and distinguishing dysplastic from normal tissues[82,86]. In order to center the catheter in the relatively large lumen of the esophagus, balloon catheters have been developed to enable reproducible circumferential scanning.

The first *in vivo* demonstration of intracoronary OCT imaging in human was performed in 2001, demonstrating diagnostic imaging of arterial wall pathologies and coronary interventions[56]. Since then, the technology has become commercially available. It is primarily used for inspection of stents and for diagnosing unstable forms of coronary atherosclerosis[87-92]. For intravascular imaging, the primary challenge is to clear the strongly scattering red blood cells. An efficient clinical solution is to displace the blood temporarily by flushing the artery with saline or x-ray contrast dye[79,83,88,89,93].

OCT depends on a spatially coherent wavefront, the shape of which determines the point spread function. Image quality, in terms of contrast and resolution, benefits from a well-characterized, round beam shape. In endoscopic applications in particular, controlling the wavefront can be a challenge because of the limited space available for the optics in the probe. In this study, we characterize the effect of endoscope optical design and discuss strategies for optimization of the beam characteristics for imaging.

5.1.2 | Astigmatism introduced by the catheter outer tube
A transparent protective tube is commonly applied on the outside of the catheter. This tube isolates the tissues under investigation from rotating catheter parts, guides the pullback motion, and protects the catheter inside from blood and mechanical damage. However, while effectively separating tissue and device, the tube acts as a negative cylindrical (concave/convex) lens, contributing to divergence of the light beam in one direction[94-98]. As illustrated in Fig. 1, the beam waists are different in vertical and

5

horizontal direction of light beam, and are found at different locations: the beam becomes astigmatic. The extra divergence will lead to a decrease in transverse resolution, image contrast, and Strehl ratio[94-96]. A long working distance (distance from focal point to optical axis of the device), required for esophageal imaging, or a liquid environment, as in intracoronary imaging, aggravate the problem. In these cases, the additional divergence should be taken into consideration for catheter design.
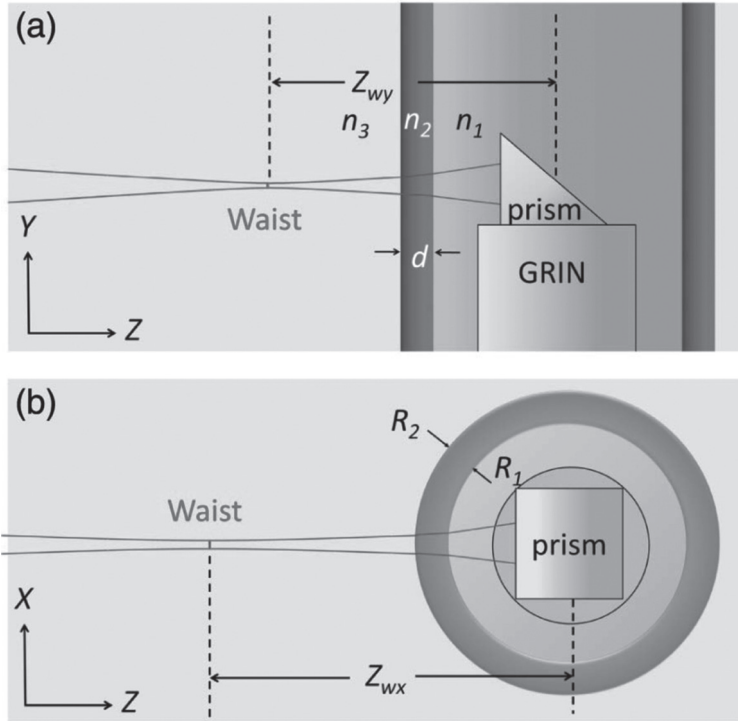
Figure 5.1 | Schematic diagram of imaging catheter tip, shown in (**a**) side view; (**b**) top view. n_i: index of inner medium, n_2: index of tube, n_3: index of outer medium, R_1: inner radius of tube, R_2: outer radius of tube, d: thickness of tube, z_w: working distance (z_{wx} in azimuthal direction, z_{wy} in longitudinal direction).

The astigmatism of the beam (and the resulting point spread function) is not necessarily evident from the acquired data. Particularly in coronary imaging, the artery under investigation is routinely sampled with a frame pitch of 200 μm, much larger than the spot size in either direction. The imaged volume is grossly undersampled in the pullback direction.

In previous studies, Xi *et al.*[96] and Kang *et al.*[97] described a correction method for long working distance endoscopes, to refocus the light beam along one direction with a cylindrical mirror or prism to approach a circular beam profile. Swanson *et al.*[55] provided another method based on matching the refractive index for imaging in a fluid environment.

In the present paper, we will quantify the astigmatism based on optical simulations and provide a systematic way to optimize the beam compensation in different catheter types.

5.2 | Methods

5.2.1 | Probe optical design and geometry

The common optical design, widely applied in both esophageal and coronary OCT imaging, is to focus the Gaussian beam emitted from a single mode fiber (SMF) using a gradient refractive index (GRIN) lens[55,85,93,96,97,99-101].

In our simulations, we assume the imaging beam is perpendicular to the catheter, neglecting the small offset angle that is usually chosen to reduce sheath reflections. We will adopt the following terminology for the beam parameter coordinates, see also Figure 5.1. The spot is described in cross section (x, y) plane perpendicular to the direction of beam (z). The x-axis of the plane is chosen in the image plane, perpendicular to catheter, and is called the "azimuthal" direction, as it coincides with the rotation direction of the catheter. The y-axis is parallel to the catheter, and is called the "longitudinal" direction, as this is the pullback direction, and the longitudinal direction of the luminal organ under investigation.

The transparent tube enclosing is commonly made in flexible optical transparent plastic such as Fluorinated Ethylene Propylene (FEP) or Polyethylene (PE). As illustrated in Figure 5.1, the light beam defocuses in x-z plane as a common negative effect in almost all side-view OCT probes. The ray transfer matrixes of the tube are showed as follows respectively in two directions:

In the x-z (image) plane:

$$\begin{pmatrix} 1 & 0 \\ \dfrac{n_2-n_3}{R_2 n_3} & \dfrac{n_2}{n_3} \end{pmatrix}\begin{pmatrix} 1 & d \\ 0 & 1 \end{pmatrix}\begin{pmatrix} 1 & 0 \\ \dfrac{n_1-n_2}{R_1 n_2} & \dfrac{n_1}{n_2} \end{pmatrix} = \begin{pmatrix} 1+d\dfrac{n_1-n_2}{R_1 n_2} & \dfrac{dn_1}{n_2} \\ \dfrac{n_2-n_3}{R_2 n_3}+\dfrac{d\left(n_2-n_3\right)\left(n_1-n_2\right)}{R_1 R_2 n_2 n_3}+\dfrac{n_1-n_2}{R_1 n_3} & \dfrac{n_1}{n_3}+\dfrac{dn_1\left(n_2-n_3\right)}{n_2 n_3 R_2} \end{pmatrix}. \quad (1)$$

In the y-z plane (containing the catheter):

$$\begin{pmatrix} 1 & 0 \\ 0 & \dfrac{n_2}{n_3} \end{pmatrix}\begin{pmatrix} 1 & d \\ 0 & 1 \end{pmatrix}\begin{pmatrix} 1 & 0 \\ 0 & \dfrac{n_1}{n_2} \end{pmatrix} = \begin{pmatrix} 1 & \dfrac{dn_1}{n_2} \\ 0 & \dfrac{n_1}{n_3} \end{pmatrix}. \quad (2)$$

The resultant working distance z_w and beam waist w_0 will be calculated in x and y directions; designated by appropriate subscripts.

5.2.2 | Simulation

In order to simulate the astigmatism effect and the compensation methods, we applied a model of a GRIN lens based catheter including commercial available GRIN lens (g = 1.372 mm⁻¹ and 0.636 mm⁻¹) and a glass spacer, single mode fiber (mode field diameter = 9.2 μm at 1310 nm wavelength), a plastic tube and a reflect mirror (or a prism). The parameters of the GRIN lens and glass spacer are first calculated by paraxial Gaussian beam analysis. The Gaussian beam can be characterized by two parameters: the beam waist (w_0) and the distance from reference plane to beam waist, which can be expressed by the complex beam parameter q[102]:

$$q_1 = Z + Z_R i = Z + \frac{\pi n_m w_0^2}{\lambda} i, \tag{3}$$

where Z denotes the distance from the beam waist to the reference plane; Z_R is the Rayleigh length; w_0, the beam waist; λ, the wavelength; and n_m is the refractive index of the propagation medium. An optical system can be characterized by the ray transfer matrix (ABCD matrix). The Gaussian beam, defined at the entrance by q_1, is transformed by the optical system as[102]:

$$q_2 = \frac{Aq_1 + B}{Cq_1 + D}. \tag{4}$$

If the ray transfer matrix is known, one can adjust the parameters of output Gaussian beam in focal length and beam waist by manipulating the elements of the ABCD matrix. The equivalent ABCD matrix describing the propagation of a Gaussian beam in a GRIN lens is given by[103]:

$$\begin{pmatrix} A & B \\ C & D \end{pmatrix} = \begin{pmatrix} 1 & f \\ 0 & 1 \end{pmatrix} \begin{pmatrix} 1 & 0 \\ 0 & \dfrac{n_g}{n_m} \end{pmatrix} \begin{pmatrix} \cos(gl_g) & \dfrac{\sin(gl_g)}{g} \\ -g\sin(gl_g) & \cos(gl_g) \end{pmatrix} \begin{pmatrix} 1 & 0 \\ 0 & \dfrac{n_s}{n_g} \end{pmatrix} \begin{pmatrix} 1 & l_s \\ 0 & 1 \end{pmatrix} \begin{pmatrix} 1 & 0 \\ 0 & \dfrac{n_f}{n_s} \end{pmatrix}. \tag{5}$$

Here, n_f is the refractive index of the fiber, n_g denotes the axial refractive index of GRIN lens, l_g is the length of the GRIN lens, g is the gradient constant of the GRIN lens, n_s is the refractive index of the spacer, l_s is the length of the spacer, and f is the focal length of the lens.

The focal length (f), and beam waist ($w_0 w$) of the output beam can be related to the GRIN lens and spacer parameters, and the mode field radius of the single-mode fiber (w_s)[101]. These relations can be solved for l_g and l_s to yield the optimal lengths of the GRIN lens and spacer given the desired focal length and beam waist for a specific application. The parameters calculated based on the paraxial Gaussian matrix transformation will be further optimized by physical optics formalism as implemented in Zemax2008 (ZEMAX Development Corp., WA, USA) to obtain a better approximation. We quantify the astigmatism by the spot ellipticity of the output beam. In particular, the optical surfaces that are not

collinear with the optical axis cannot be accurately modeled using the Gaussian paraxial approximation. The compensation performed on the esophageal and coronary imaging simulation models will also be evaluated by applying the physical optics formalism for better approximation.

5.2.3 | Catheter model for esophageal imaging

The balloon used for esophageal imaging commonly has a diameter of 20 mm. Consequently, most of the published balloon catheter designs have a working distance of 9-12 mm. Spot sizes range from 15-40 µm. The properties of output light beam are mainly related to the maximum beam diameter (MBD) within the GRIN lens. A long working distance requires long focal length which means the MBD needs to be expanded to maintain a small beam waist. This can be achieved in different ways: one is to expand the input spot size at the GRIN lens by increasing the spacer length l_s[100]. Another is to increase the divergence of the input beam by decreasing its waist, which can be realized by applying another GRIN lens between SMF and spacer[96,101]. While expanding the beam within the GRIN lens, the MBD should be limited to 80% of the lens aperture to ensure the beam profile remains Gaussian. In our simulation model, we applied a model of a single GRIN lens probe as shown in Figure 5.2. The light beam, coming from an SMF28 fiber, is expanded by a 3.7 mm length glass spacer (n_s = 1.5) before entering a 0.7 mm length, 1.0 mm diameter GRIN lens (g = 0.636 mm^{-1}); A mirror is at 2 mm distance from the GRIN lens, and deflects the light beam to an FEP tube (R_l = 0.75 mm, d = 0.1 mm). The simulation shows that the ideal working distance z_w = 11.25 mm) and form a waist of 23.1 µm.
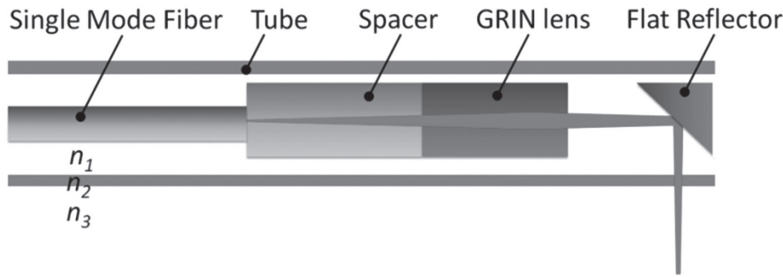
Figure 5.2 | Schematic diagram of the simulation model of a GRIN lens-based OCT probe with a reflector; n_1: index of inner medium, n_2: index of tube, n_3: index of outer medium

5.2.4 | Catheter Model for Coronary Imaging

For cross-sectional visualization of the entire coronary artery (diameter: 3-4 mm) with sufficient resolution, a relatively short working distance (approximately 1-2 mm) and long depth of field (preferably > 2 mm) are necessary, nevertheless, at the cost of increasing the beam waist which is commonly 20-30 µm[55,88]. In practice, the outer diameter of a coronary imaging catheter is limited to 1 mm or slightly more, including the protective tube[55,93].
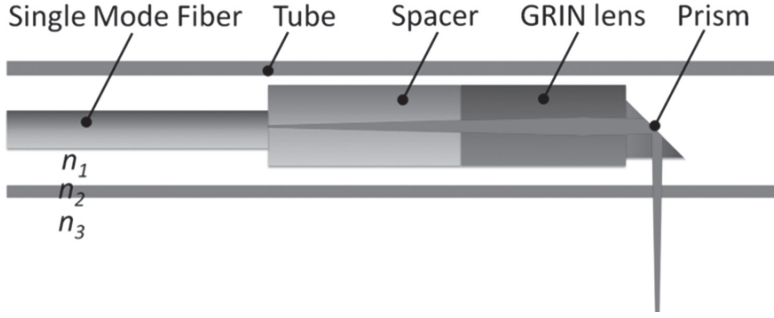
Figure 5.3 | Schematic diagram of simulation mode for a GRIN lens-based OCT probe with a prism; n_1: index of inner medium, n_2: index of tube, n_3: index of outer medium

In our work, we applied a probe model, as shown in Figure 5.3, which is a typical design based on a GRIN lens. A high gradient constant GRIN lens ($g = 1.372$ mm^{-1}) attached to a prism is used to shorten the length of rigid part. Parameters were set as: GRIN lens (diameter = 0.50 mm, $l_g = 1.10$ mm, $g = 1.372$ mm^{-1}), Glass spacer (diameter = 0.50 mm, $l_s = 0.14$ mm, $n_s = 1.50$). Microprism ($n = 1.50$, length of short side = 0.35 mm), FEP Tube ($R_1 = 0.40$ mm, $d = 0.10$ mm). The simulation shows that the ideal light beam attains a focus at $z_w = 1.46$ mm and forms a 20.8 μm beam waist.

For coronary imaging, the optics of the OCT beam will be affected by the refractive index of the flush medium in the artery, which is used to displace the blood. The specific media that are commonly used, and that we will also use in this paper, are saline ($n_3 = 1.33$) and the contrast dye Iodixanol 370 (Visipaque, GE Healthcare; $n_3 = 1.45$).

5.2.5 | Minimization of the Astigmatism

For optimal image quality, the beam shape should be as round as possible along the light path, which means the beam parameters in azimuthal and longitudinal directions should be equalized by correcting the working distance and beam waist in the azimuthal direction, targeting those in the longitudinal plane. Ideally, the compensation for laser astigmatism can be realized by a pair of interfaces such as cylindrical lens or an anamorphic prism. Two curved surfaces are needed in general, because both the beam size and the divergence need to be compensated, and these parameters are not independent if only one cylindrical surface is applied.

We compute the optimal compensation by setting the beam parameters at the focus to the desired ones and backpropagating the beam through the tube and the catheter optics to compare both beam directions at a reference surface. The compensation is simulated in the azimuthal direction, aiming to refocus the light beam back to the target focal point, and adjusting the radius of curvature R_c of the correcting surface to achieve optimal focusing. The optimization is performed on the spot deviation, which is the absolute value of difference between spot ratio and 1, integrated over the Rayleigh range:

$$\Delta_w = \int_{z_w-z_R}^{z_w+z_R} \left| w_x(z)/w_y(z) - 1 \right| dz, \tag{6}$$

where z_w is the target working distance, z_R is the Rayleigh length, and $w_x(z)$ and $w_y(z)$ are the spot sizes with distance z from the optical axis, respectively in the azimuthal and longitudinal directions. The beam is optimized when this integral is minimized.

5.3 | Results

5.3.1 | Characterization of Astigmatism

In order to characterize the astigmatism introduced by the tube, we calculated the spot size at the target focal plane in the azimuthal direction, with different parameters based on paraxial Gaussian formalism, including tube material and dimensions, and design the working distance of the light beam. Calculations were performed with air as outer and inner media.

The results are shown in Figure 5.4. A thick-walled tube made of high-index material, such as polyethylene (PE), causes stronger astigmatism. Use of a thin-walled tube, made of low-index material, minimizes astigmatism; under these conditions, the ray transfer matrices approach the same limit in two directions. For a short working distance probe, the effect is well controlled in this manner; for instance: for $R_1 = 0.5$ mm, with $d = 0.05$ mm, $z_w = 2$ mm, and $w_0 = 20$ μm, the spot size at the target focal plane will be $w_x = 22.2$ μm in the azimuthal direction after an FEP tube is applied. In contrast, the spot size expands quickly with increasing thickness of the tube, particularly for long working distance probes.
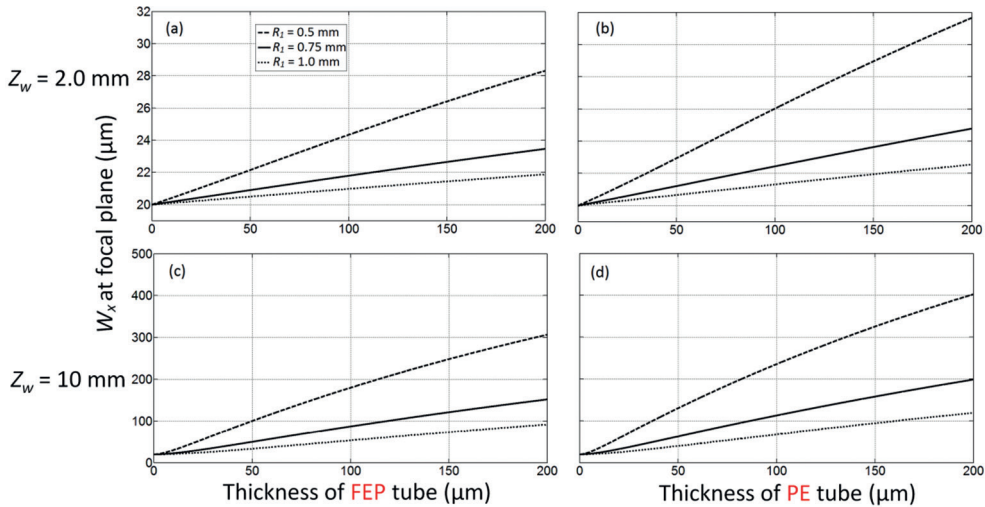
Figure 5.4 | Dependence of the spot size at the target focal plane in the azimuthal direction on the thickness of the tube for different inner radius (R_1). (**a**) and (**b**): short working distance (z_w = 2.0 mm); (**c**) and (**d**): long working distance (z_w = 10 mm). (**a**) and (**c**): Fluorinated Ethylene Propylene (FEP) tube (n_2 = 1.34); (**b**) and (**d**): Polyethylene (PE) tube (n_2 = 1.50). The beam waist was set to be w_0 = 20 μm; n1 = n_3 = 1.0.

The application of endoscopic catheters in a liquid environment further aggravates the astigmatism. As shown in Figure 5.5, the spot size in the azimuthal direction increases quickly with increasing index of the outer medium.
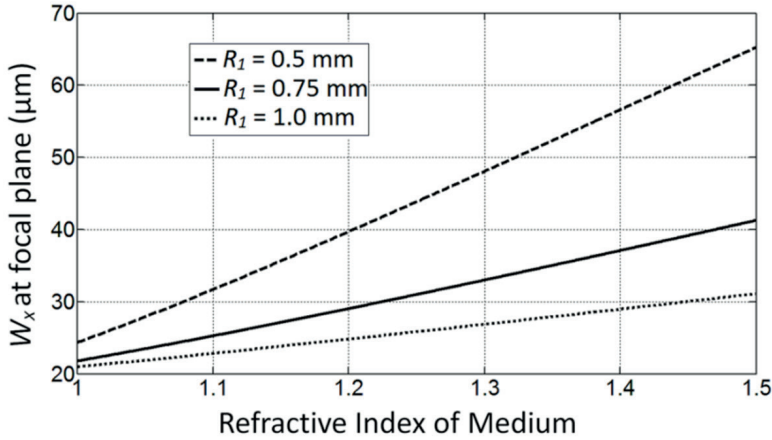
Figure 5.5 | Plot of spot size at focal plane in azimuthal direction versus refractive index of medium with various inner radius (R_1) of tube, made of 0.1 mm thickness FEP ($n = 1.34$). $z_w = 2.0$ mm; $w_0 = 20$ μm.

5.3.2 | Astigmatism of Esophageal Imaging Catheters

The long working distance results in a relatively large spot size on the tube wall, which enhances the defocusing effect of the cylindrical tube. Figure 5.6 shows the astigmatic beam and the spot profile at the target focal plane. This design achieves $z_{wy} = 11.25$ mm and $w_{0y} = 23.1$ μm in the longitudinal direction. Due to the defocusing effect of the tube, the working distance in the azimuthal direction will be shifted to $z_{wx} = 19.95$ mm, forming a waist w_{0x} of 41.7 μm. At the target focal plane, the spot size in the azimuthal direction w_x is nearly 100 μm, whereas $w_y = w_{0y} = 23.1$ μm. As the spot expands, the energy of the spot spreads from center to periphery, which reduces the irradiance peak value by a factor of 3. Lower irradiance peak value will reduce the magnitude of the impulse response (point spread function) in the lateral direction, and thus lead to degradation in image contrast.
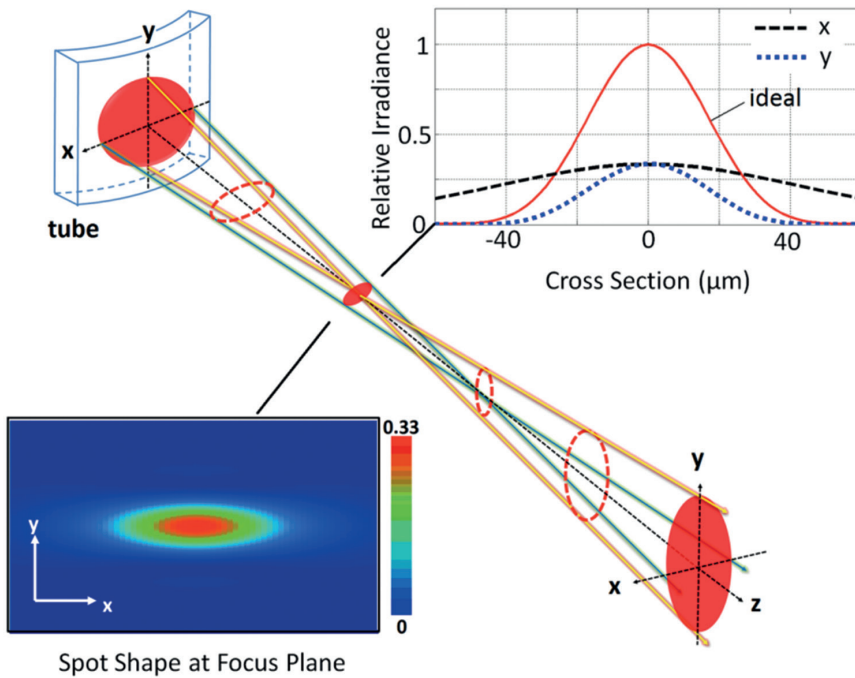
Figure 5.6 | The irradiance profile of the astigmatic beam emitting from the tube with spot profile at target working distance. The scale bar is 50 μm; *x*: azimuthal direction, *y*: longitudinal direction.

5.3.3 | Optimal Compensation for Esophageal Imaging Catheters

The backpropagated spot size in the azimuthal direction inside the tube is shown in Figure 5.7, compared to the desired beam dimension. The azimuthal spot size of the light beam is close to the desired spot size within the tube and is identical to the desired one at plane A. At this location, the compensation can be achieved to a good approximation with single cylindrical interface, using a cylindrical mirror or cylindrical lens to correct the divergence; spot size correction is not needed not needed here[104]. Conversely, at at plane B, both diameter and divergence of the beam need to be corrected and two cylindrical surfaces are required.
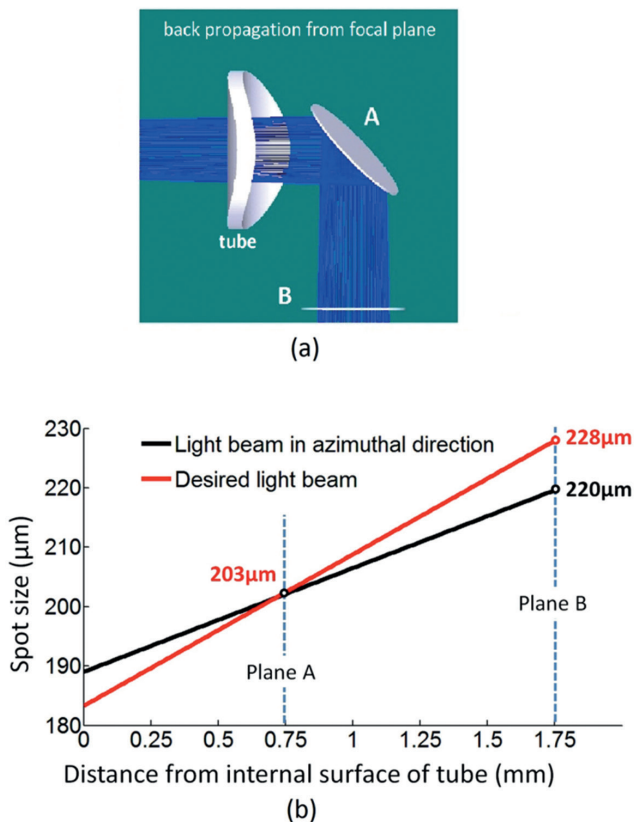
Figure 5.7 | (a) Schematic of Gaussian beam inside the tube, back-propagated from the focal plane, for a long working distance catheter: the interfaces of the mirror and lens are located at plane A (the reflector) and plane B (the distal lens surface) respectively. (b) Spot sizes of the Gaussian beam in azimuthal direction and the desired light beam varying with distance from the internal surface of the tube. The distances from the tube to the compensation planes are: A 0.75 mm, B 1.75 mm

Figure 5.8 shows two compensations performed with a cylindrical mirror at plane A and a cylindrical lens at plane B, respectively. The reflector in Figure 5.2 is replaced by a cylindrical one in Figure 5.8(a): the cylindrical interface is applied at plane A as shown in Figure 5.7(a). Alternatively, a cylindrical lens is used in Figure 5.8(b) with the correcting surface located at plane B.
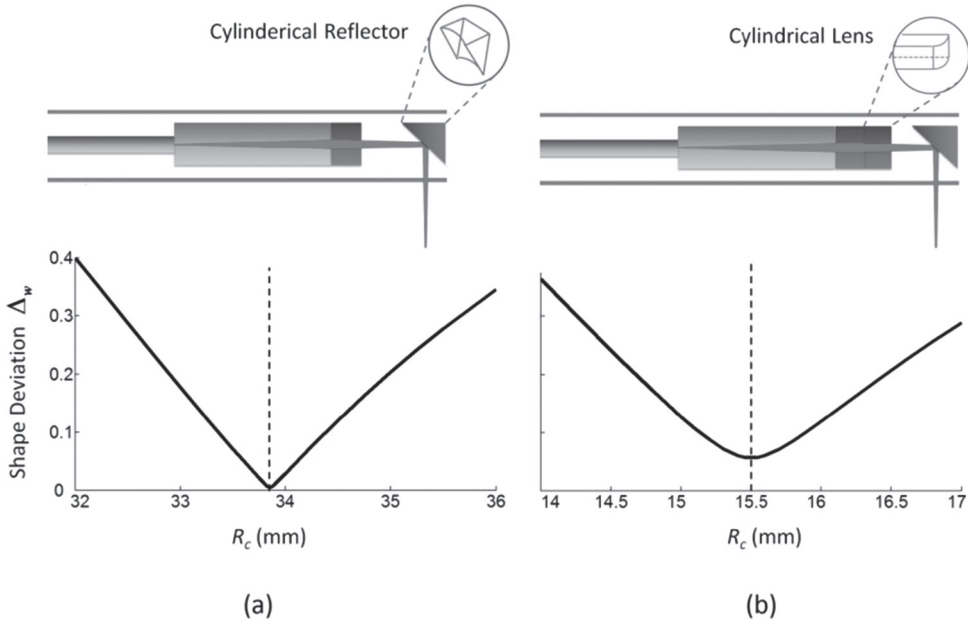
Figure 5.8 | Schematic diagrams of simulation mode for a GRIN lens probe with (**a**) a cylindrical mirror and (**b**) a cylindrical lens. Near-perfect correction is achieved using a cylindrical mirror in plane A. GRIN lens diameter: 1 mm, l_g : 0.7 mm, g: 0.636 mm^{-1}; glass spacer l_s: 3.7 mm, n_s : 1.5. R_c: Curvature Radius.

The compensation results are shown in Table 5.1. The light beam is efficiently refocused back to the target working distance, while the working distances in both directions are almost identical after compensation. A round spot shape with ellipticity w_x / w_y = 1.00 is achieved with cylindrical mirror compensation, whereas w_x / w_y = 1.04 with cylindrical lens compensation. The small remaining astigmatism when applying a cylindrical lens is due to use of only one interface for correction at plane B rather than two.

Table 5.1 | Beam characteristics for an esophageal imaging probe, and two compensation methods. Design working distance z_w = 11.25 mm; beam waist w_0 = 23.1 µm. Compensation parameters: cylindrical lens: BK7 glass, thickness 1.5 mm, radius of curvature R_c = 15.5 mm; cylindrical reflector R_c = 35.7 mm.

		No compensation	Cylindrical lens	Cylindrical reflector
Working distance z_w	z_{wx} (mm)	19.95	11.25	11.25
	z_{wy} (mm)	11.25	11.25	11.25
Spot size at z_w	w_x (µm)	96.5	24.0	23.2
	w_y (µm)	23.1	23.1	23.1
Ellipticity	w_x/w_y	4.17	1.04	1.00

5.3.4 | Astigmatism of Coronary Imaging Catheters

An intracoronary imaging catheter is immersed in fluid while imaging. The curved inner surface of the (air-filled) tube now has a significantly higher optical power than the outer surface, which is partially index-matched by the fluid surrounding the catheter, inducing strong astigmatism. Table 5.2 shows the dependence of the spot profile on the distance from the tube in air, saline, and Visipaque, respectively. In air, though slightly defocused, the light beam can still form a waist of $w_{0x} = 25.1\mu m$ waist at $z_{wx} = 1.51$ mm, versus $w_{0y} = 20.8$ µm at $z_{wy} = 1.46$ mm.

For higher refractive index of the external medium, the defocusing effect of the tube becomes progressively stronger, and finally results in a total defocusing light beam in the azimuthal direction for n > 1.15. The spot size in the azimuthal direction continuously expands with increasing distance, while the light beam in the longitudinal direction is focused at 1.81 mm working distance in saline, and at 1.89 mm in Visipaque, with the same beam waist as target.

Table 5.2 | Spot shape with various distances (z) from optical axis, respectively in air, saline and Visipaque. Data in the emitting plane is independent of imaging media. The Rayleigh plane is located at the Rayleigh distance in the y-direction.

		Emitting plane	Target focal plane	Rayleigh plane
In air (index: 1.0)	z (mm)	0.50	1.46	2.50
	w_x at z (µm)	30.2	25.1	30.0
	w_y at z (µm)	28.3	20.8	29.4
	ellipticity	**1.07**	**1.21**	**1.02**
In Saline (index: 1.37)	z (mm)		1.81	3.24
	w_x at z (µm)		44.7	62.8
	w_y at z (µm)		20.8	29.4
	ellipticity		2.15	2.13
In Visipaque (index: 1.45)	z (mm)		1.89	3.39
	w_x at z (µm)		49.2	71.5
	w_y at z (µm)		20.8	29.4
	ellipticity		2.37	2.43

5.3.5 | Compensation for Coronary Imaging by a Cylindrical Interface

In order to maintain a round spot profile at the focal plane, we applied single cylindrical interface to make the compensation. The simulation is performed with a probe immersed in Visipaque. The deviation between the azimuthal spot size and the target, shown in Figure 5.9, increases rapidly with distance from the internal tube surface. This situation is unlike the case of the esophageal catheter, where a plane with the desired beam profile could be identified for effective, single curvature correction.
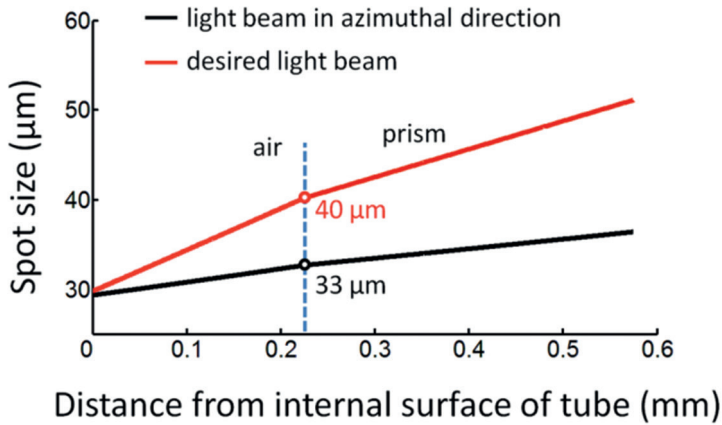
Figure 5.9 | Plot of spot size in Visipaque of the back-propagated light beam, versus distance to internal surface of tube. The distance from the prism exit surface to the tube is 0.225 mm.

In the intracoronary catheter, the compensation interface should be applied as close as possible to the internal surface of the tube to match the curvature. This can be approximated by replacing the emitting plane of the prism by a cylindrical one, as shown in Figure 5.10, which is more effective than replacing the inclined reflecting surface by a cylindrical one. Because the light beam is strongly defocused in the azimuthal direction by the interface of the tube, immersed in Visipaque, the back-propagated light beam in the azimuthal direction is much smaller than required. Limited by this small spot size, the light beam cannot be focused back to the target focal point by a single cylindrical interface without magnifying the beam. With single cylindrical interface compensation, the difference in spot size will persist and manifest itself as a deviation not only in beam waist but also in working distance between the two directions.

Our simulation shows that the optimal correction is achieved with a radius of curvature $R_c = 0.75$ mm. After correction, the light beam in the azimuthal direction will focus at $z_{wx} = 1.89$ mm distance and form a beam waist $w_{0x} = 21.1$ μm. As shown in Table 5.3, although convergence in the azimuthal direction has been restored, effectively improving the beam, the beam remains astigmatic.

5
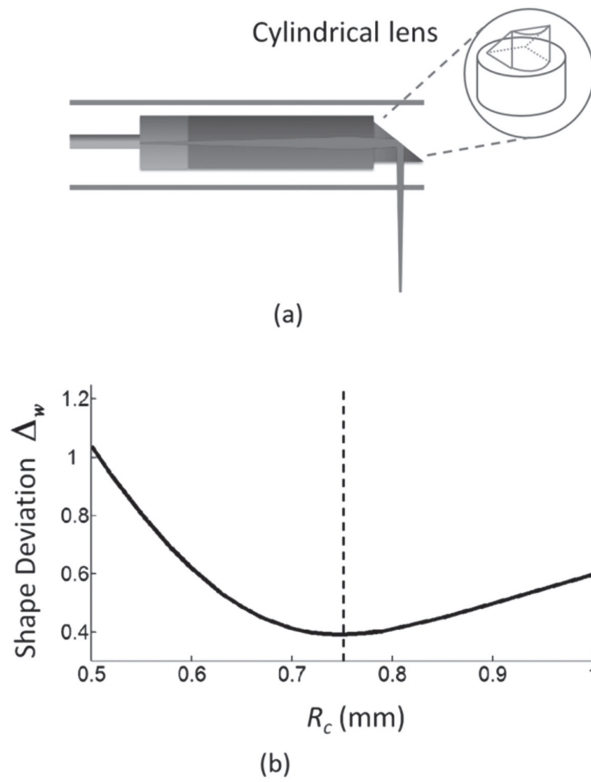
Figure 5.10 | Schematic diagrams of simulation mode for a GRIN lens probe with a cylindrical lens mounted on the prism. The integral reaches its minimum value when the curvature radius is 0.75 mm. The parameters of GRIN lens and spacer are the same as Figure 5.7. R_c: Curvature Radius.

Table 5.3 | Characteristic of light beam after compensation showed as spot shapes in Visipaque. The Rayleigh plane is located at the Rayleigh distance in the y-direction.

		Emitting plane	Target focal plane	Rayleigh plane
Without compensation	z (mm)	0.50	1.89	3.39
	w_x at z (μm)	30.2	49.2	71.5
	w_y at z (μm)	28.3	20.8	29.4
	ellipticity	**1.07**	**2.37**	**2.43**
Curved interface	z (mm)	0.50	1.89	3.39
	w_x at z (μm)	23.4	22.8	36.1
	w_y at z (μm)	28.3	20.8	29.4
	ellipticity	**0.83**	**1.10**	**1.23**
Matching fluid	z (mm)	0.50	1.99	3.50
	w_x at z (μm)	28.7	19.2	30.4
	w_y at z (μm)	29.3	20.8	29.4
	ellipticity	**0.98**	**0.92**	1.03

5.3.6 | Compensation for Coronary Imaging by Index-Matching Flushing Liquid

Refractive index matching by flushing the catheter from inside with the proper index-matching liquid can effectively neutralize the effect of the cylindrical tube by driving the C element of the ABCD matrix (1) towards 0.

$$\frac{n_2 - n_3}{R_1 n_2} + \frac{d\left(n_2 - n_3\right)\left(n_1 - n_2\right)}{R_1 R_2 n_2 n_3} + \frac{n_1 - n_2}{R_1 n_3} = 0. \tag{7}$$

However, the other elements of the ray transfer matrix are still different from the longitudinal direction, which will cause a slight astigmatism after compensation. When using Visipaque to displace blood, the refractive index of the matching fluid for optimal correction will be 1.465 by calculation. As the index of fluid is very close to Visipaque (1.45), it will be convenient to use Visipaque to flush the catheter as the matching fluid. The spot shape after compensation is also shown in Table 5.3.

5.4 | Discussion

Endoscopic OCT has become a common diagnostic and research tool. Astigmatism of the imaging beam is a common side effect in sideview OCT endoscopes, which may degrade the image resolution and image contrast. Poor resolution in the longitudinal direction may not be apparent from the acquired data, because pullback OCT data are routinely undersampled in the pullback direction. In this paper, we present a quantitative analysis of the endoscope optics relating to the astigmatism, using fairly general assumptions about the catheter design. We also present a strategy for optimal compensation of the beam for specific imaging applications and geometries.

Particularly for short working distance probes working in air, the difference in optical characteristics between azimuthal and longitudinal directions can be well controlled by applying a thin-walled tube (relative to the tube diameter), made of low refractive index material. In this case the deviation from the design beam waist and working distance remain less than 10%.

Two current applications of catheter-based OCT do not operate in this limit, however. For long working distance probes, such as those used for imaging of the esophagus, and probes working in liquid, such as coronary imaging catheters, the astigmatism effect is so serious that extra compensation has to be designed. We implemented a simulation model for GRIN lens probes to evaluate the compensation methods. For catheters imaging the esophagus, with a long working distance of approximately 10 mm, our simulation demonstrates that a round spot shape can be restored by refocusing the light beam back to the focal point in the azimuthal direction with single cylindrical surface in the beam path. It is important that this surface be positioned in a plane transverse to the beam, where the uncorrected and ideal spot sizes are identical. In this case, a single curved surface suffices to adjust the beam convergence.

5

For uncompensated catheters working in a liquid environment, the beam actually becomes divergent in the azimuthal direction for $n_3 > 1.15$, which is practically for every fluid medium. In that case, compensation is more difficult than in air, as two curved surfaces are needed for full correction of the astigmatism. We demonstrated that convergence can be restored by means of a single cylindrical lens positioned as close as possible to the tube inner wall, but the beam remains astigmatic, with a deviation from the ideal spot size of 23%.

Another compensation method was also simulated by matching the refractive index inside the tube. Compared with the cylindrical interface method, the quality of spot profile along the line of sight is improved. For compatible catheter designs, fluid filling is an effective solution. Refractive index matching also has the engineering advantage in that it does not require accurately positioned curved surfaces. Drawbacks are the occasional occurrence of artifacts due to air bubbles in the flush liquid, and the requirement of an open hole in the catheter tip to maintain flush pressure inside the catheter tube during pullback. Blood may enter the catheter through the hole, which needs to be removed by flushing for repeat acquisitions.

The optimizations in this paper were performed by minimizing the integrated ratio w_x / w_y over the Rayleigh range. There are other performance measures which could be used, e.g., minimizing the difference between designed and realized working distance and beam waist. Such analysis could result in subtle differences in the end results, but the overall trend will be the same. It depends on the application requirements which measure is most appropriate.

5.5 | Conclusion

We quantified the astigmatism in endoscopic OCT probes, which is introduced by the external tube and environment media, and analyzed compensation methods based on optics simulation. Based on the analysis of the probe optics, we presented optimal compensation schemes for common catheter types. A numerical analysis of minimizing the astigmatism such as performed here can facilitate the design and optimization of OCT imaging catheters for specific applications.

Chapter 6

驭赤兔，往何处？ **Very very fast?**

Heartbeat OCT is a new modality for comprehensive imaging of the coronary vasculature *in vivo* at microscopic resolution, aimed at characterization of coronary artery disease and guidance of coronary interventions. The development of the prototype of Heartbeat OCT required research in multiple fields such as mechanical engineering, image processing, optical design and hardware control. This chapter summarizes the development of Heartbeat OCT, introduces various types of knowledge that were used and discusses the present and future impact of Heartbeat OCT on medical imaging technology and medicine.

Development and refining of a high-speed micro actuator

In recent years, distal micro actuators are of high interest for endoscopic OCT[44,54,64,71,105]. These designs have explored a variety of technological solutions for scanning a beam from a thin, flexible catheter to achieve OCT imaging of internal organs. Although often highly innovative, limitations remained in scan speed, size, or the field of view (providing forward-looking or oscillatory scans). So far, a micro actuator based catheter for intracoronary imaging has not been realized due to the limitations of the dimension and the speed.

In 1994, Charles T. Lancee *et al.* invented a synchronous micro motor in Thoraxcenter, ErasmusMC[45,46]. The micro motor was originally used to rotate an ultrasound element in IVUS catheter. In 2012, a new model of the micro motor was manufactured specifically for Heartbeat OCT. With a size of 2.0 mm length and 1.0 mm OD, the motor is suitable for intravascular imaging. Furthermore, the new model can rotate at speeds of several thousand revolutions per second, with high uniformity and low angular position error. To the best of our knowledge, the micro motor has the smallest dimension and the highest rotating speed among the actuators for endoscopic imaging. It also requires a relatively low power to reach a much higher speed than any other actuator (Chapter 2).

The micro motor enables a new beam scanning modality that has several advantages compared to conventional methods. The micro motor can rotate a mirror at the catheter tip to realize the beam scanning while the fiber probe itself remains stationary. Since the torque transfer and the friction of the rotating fiber are avoided, the beam-scanning performance depends on the rotating situation of the motor only. Therefore, a much higher beam scanning speed was achievable and the NURD issue was solved. The rotation behavior, power consumption, friction and torque of the motor were characterized and found to be suitable for integration into a catheter.

First prototype of Heartbeat OCT imaging at 3200 fps *in vitro*

An intravascular catheter was manufactured within 1.1 mm OD, using the new model of the micro motor as the distal actuator. As a traditional optical design, a GRIN lens and a mirror were used to focus and deflect the light beam. We built the first prototype of Heartbeat OCT by combining the intravascular

catheter with an FDML laser working at 1.6 MHz. With the first prototype, it is possible to image human coronary arteries in a laboratory setting. *In vitro* experiments were conducted in human LAD by running the system at 3200 fps and 100 mm/s pullback speed. At that moment, the maximum imaging speed of endoscopic OCT was still limited to a few hundred fps. The *in vitro* results showed that the high-speed imaging significantly improves the quality of longitudinal rendering (Chapter 3). The IV-OCT system also showed its potential to finish imaging of an artery within one cardiac cycle.

Second prototype of Heartbeat OCT imaging at 5600 fps *in vitro* and 4000 fps *in vivo*

To apply Heartbeat OCT in *in vivo* imaging, two main improvements needed to be done: further increasing the speed of the motor and improving the flexibility of the catheter. A low viscosity oil was applied to the micro motor, leading to a much higher rotating speed. The flexibility of the catheter was improved by using a Pebax tube as the sheath of the entire catheter. A shorter prism holder also reduced the rigid length to 2.0 mm. Besides the intravascular catheter, an FDML laser was also developed, of which the maximum sweep rate is 2.88 MHz. With 1.0 A driving current, the second prototype provided up to 5600 fps speed that can be used for *in vitro* imaging. We demonstrated *in vivo* imaging of swine coronary arteries by running the Heartbeat OCT at 4000 fps with a driving current of 0.7 A. To the best of our knowledge, the 4000 fps *in vivo* imaging speed set a new record of IV-OCT. The *in vivo* results showed that Heartbeat OCT could generate faithful and clear longitudinal rendering and 3D reconstruction, overcoming three limitations of traditional IV-OCT:

– The high imaging speed enabled the imaging procedure to be finished within one cardiac cycle, minimizing cardiac motion artifacts.
– The beam scanning modality of the catheter practically eliminated the NURD issue while providing high speed beam scanning.
– The frame rate was high enough, even at the record pullback speed of 100 mm/s, to permit a reduction of the frame pitch to < 30 μm, which was the lateral width of the point spread function.

6

It was the first time that OCT images free of NURD, cardiac motion artifacts and under sampling issues were available for *in vivo* intravascular imaging (Chapter 4).

Astigmatism study for intravascular catheter

Astigmatism is a common issue that affects the beam shape in almost all endoscopic OCT catheters. Several studies have demonstrated its negative effects and proposed some compensation methods in the field[96,101]. To better understand the astigmatism effect and evaluate all possible compensation methods, a systematic numerical analysis is necessary, which is also helpful to optimize the optical design of Heartbeat OCT. Optical simulation was conducted with several models of various types of endoscopic catheters. The simulation results demonstrated that the negative effect was more serious in catheters in a liquid environment than those in an air environment. The numerical analysis also showed that focusing the light beam by a curved mirror/prism could commonly compensate the astigmatism. Though index-matching compensation could fully overcome the astigmatism, it cannot be applied to Heartbeat OCT at the moment, since such method is not compatible with the micro-motor-based design (Chapter 5).

Future development of Heartbeat OCT

Further minimization of the motor should allow a catheter with smaller dimensions. As a practical solution, the outer tube of the catheter can be used as the sheath of the motor. The catheter and the motor will be united, and the outer diameter can be reduced to < 1.0 mm. For clinical application, a guide wire is used to direct the catheter to distal arteries. Using a guide wire greatly improves deliverability of the catheter, especially when inserting the catheter through small lumens or stents, and reduces vessel trauma. However, stainless steel guide wires can affect the rotation of the micro motor due to the magnetism between the permanent magnet rotor and the iron in the guide wire. Nitinol wires are non-magnetic and hence should not interfere with the driving field in the motor. These guide wires are becoming more common. However, if a nitinol wire cannot be used, the motor housing may be replaced by antimagnetic material or a magnetically soft material. The motor leads can be further reduced to 50 μm thickness and twisted to minimize the impact of the motor leads shadow.

Further improving the image quality of Heartbeat OCT requires a compensation for the astigmatism. Since index-matching methods are not suitable for the current micro-motor-based design, the practical solution is using a curved prism/mirror to focus the light beam in the azimuthal plane. Without the negative effect caused by astigmatism, the imaging contrast and the viewing depth can be both improved. Even though the current catheter design doesn't require a rotating fiber probe, the fiber is slightly stretched during pullback, which may change the optical length in the sample arm. To solve this, a spring can be attached outside the fiber probe to protect the fiber and prevent any stretching.

FDML lasers show promising performance at high sweeping speed. However, better dispersion compensation could further improve the coherence properties in the future. Automatic frequency, offset, and range control can lead to a better stabilization than manual alignment. To improve polarization control, besides putting a spring around the fiber probe, a polarization insensitive interferometer can be applied to maintain coherence during fast pullback.

With the implementation of these final engineering steps, clinical evaluation will start its exploration of the full potential of Heartbeat OCT.

Contributions to the field of IV-OCT

Several studies have attempted to overcome the under-sampling issues and cardiac motion artifact in IV-OCT[37,106,107]. For instance, a study used a Doppler interferometer to compensate the motion artifact, but the method was not capable of eliminating the artifact[107]. Another study demonstrated an IV-OCT system providing a speed of 350 fps in 2013, which is the highest imaging speed using conventional catheter[37]. Although the imaging speed was increased in the system, however, high-speed pullback and low frame spacing were not achieved at the same time. Regarding the NURD issue, various types of micro actuators have been developed to realize the beam scanning at the catheter tip. However, none of these micro actuators can be applied into *in vivo* intracoronary imaging.

Heartbeat OCT, as a new generation of IV-OCT, provides comprehensive *in vivo* imaging of the artery at micron-order resolution, aimed at characterization of CAD and guidance of coronary interventions. By combining an FDML laser and the micro motor catheter, the imaging speed (5600 fps *in vitro* and 4000 fps *in vivo*) of Heartbeat OCT is >25 times greater compared to commercial systems[39], > 10 times over the fastest conventional system[37] and ~10 times over any other endoscopic OCT[54]. This gain in acquisition speed has two main advantages. The first advantage is a fast pullback scan of an artery that can now be performed within one cardiac cycle. The second advantage is the elimination of cardiac motion artifacts and undersampling issues at the same time. The small frame spacing allows identification of microscopic structures in the longitudinal views and 3D reconstruction, e.g. stent cells, dissection and atherosclerotic plaques. The new beam scanning modality employed by the micro motor also overcomes artifacts related to non-uniform rotation.

The micro motor catheter eliminates the need for a fiber-optic rotary junction, which overcomes both the optical and mechanical limitations. The micro-motor-based catheter design opens opptunities for advanced imaging techniques, e.g. combined OCT-fluorescence[76] or polarization-sensitive OCT[77], that offer new possibilities for tissue characterization. The parametric OCT analyses, such as Doppler OCT[78], tissue type imaging[79] or elastography[80]. relies on high-quality data. The large line density in the images provided by Heartbeat OCT will positively impact these techniques.

6

Contributions to PCI treatment

In clinical applications, PCI treatment requires an accurate choice of strategy including the sizing and positioning of therapeutic devices. For instance, a side branch can be used as a reference to implant a stent, which requires a reliable length measurement of the area of interest. However, cardiac motion affects the accuracy of length measurement, which may lead to sub-optimal positioning or sizing of the stent. Heartbeat OCT opens completely new perspectives for such decision-making. By providing reliable motion-free visualization of the vessel wall, Heartbeat OCT can take image-guided PCI to a more accurate level. Besides the PCI guidance, Heartbeat OCT also enables more clearly visualizations of post-intervention features such as dissections[72] and stent strut malapposition[73]. Artifact-free visualization of any dissections or other procedure-related vessel trauma can be critical for decision-making on whether to perform further interventions to avoid acute and long-term complications.

A conventional IV-OCT pullback requires a ~5s at 3 ml/s flush of the artery using nephrotoxic medium. Although flush amount is deemed acceptable in current clinical practices., the contrast media still introduce burden to kidneys, especially in long procedure and for patients with extensive comorbidity. The Heartbeat OCT reduces the amount of contrast media to three times less, which will enhance the acceptance of use of IV-OCT in interventional cardiology.

IV-OCT guidance provides the highest quality visualization of CAD and cardiac catheterizations. The new mode of performing IV-OCT, Heartbeat OCT, can provide the most reliable images to date. High-speed scanning will eliminate common imaging artifacts, while technology take-up by industry is encouraged by the advantages. Better, faster IV-OCT means more reliable, more accessible IV-OCT, guiding more PCI procedures to a successful outcome. If that can be achieved, repeat revascularization will no longer be necessary. Minimally invasive intervention will become available to larger patient groups, who will then not have to go to (expensive, traumatic and debilitating) open-chest surgery. This trend has started to materialize already: while coronary artery bypass graft (CABG) surgery remains the preferred treatment for patients with three-vessel CAD, PCI is emerging as a viable treatment other high-risk patient groups (left main stenosis) [108]. A reduction of the number of surgeries and repeat PCIs will be enabled and so lead to proven clinical benefit and cost effectiveness.

Outlook

The catheter and stent market currently has a volume of 8.8 billion dollar and experiences an (demographics driven) annual growth of 8%. The market share of IV-OCT as a part of intravascular imaging is growing rapidly. Overall OCT market (including ophthalmology) is 2.5 billion dollar. Approximately 500.000 intravascular imaging procedures are performed per year worldwide. With several ongoing studies poised to prove clinical benefit of invasive imaging and subsequent realization of reimbursement in all markets, there is a growth potential to >1.5 million procedures per year.

Academic research has been one of the main drivers of innovation in the medical device industry throughout the past decades. Intravascular imaging (in the form of IVUS) was an invention of the Thorax center and has been a successful imaging technology for the past 20 years. OCT itself was developed in universities in the US and Austria and has made a huge impact on ophthalmology. Heartbeat OCT contributes to translation of scientific findings directly and indirectly. The direct contribution is the creation of a collaborative structure in which university research into device innovation and medical imaging can be transferred to industry. Indirectly, the development of a better, faster IV-OCT system will promote the penetration of OCT in interventional cardiology clinics worldwide, and so enhance the dissemination of scientific insights based on OCT imaging as well as allow routine accumulation of more data. Such data, if collected in a registry, will generate the clinical science that drives image-based decision-making in therapeutic settings.

Final conclusions

IV-OCT provides high-resolution (20-30 μm), high-contrast image of the coronary artery wall and any implanted stents. However, cardiac motion artifact, NURD and undersampling affect the image quality. Based on a high-speed micro motor and a FDML laser, new generation of IV-OCT called Heartbeat OCT was developed. Heartbeat OCT achieves an imaging speed of 5600 fps *in vitro* and 4000 fps *in vivo*, which allows us to finish imaging within one cardiac cycle. Heartbeat OCT can provide comprehensive and faithful image information of coronary artery by eliminating NURD, undersampling and cardiac motion artifacts.

6

References

1. Lusis, A.J. Atherosclerosis. *Nature* **407**, 233-241 (2000).

2. Virmani, R., Kolodgie, F.D., Burke, A.P., Farb, A. & Schwartz, S.M. Lessons from sudden coronary death: a comprehensive morphological classification scheme for atherosclerotic lesions. *Arteriosclerosis, thrombosis, and vascular biology* **20**, 1262-1275 (2000).

3. Schaar, J.A., *et al.* Terminology for high-risk and vulnerable coronary artery plaques. Report of a meeting on the vulnerable plaque, June 17 and 18, 2003, Santorini, Greece. *European heart journal* **25**, 1077-1082 (2004).

4. Schaar, J.A., *et al.* Incidence of high-strain patterns in human coronary arteries: assessment with three-dimensional intravascular palpography and correlation with clinical presentation. *Circulation* **109**, 2716-2719 (2004).

5. Falk, E., Shah, P.K. & Fuster, V. Coronary plaque disruption. *Circulation* **92**, 657-671 (1995).

6. Serruys, P.W., *et al.* Percutaneous coronary intervention versus coronary-artery bypass grafting for severe coronary artery disease. *The New England Journal of Medicine* **360**, 961-972 (2009).

7. Stroupe, K.T., *et al.* Cost-effectiveness of coronary artery bypass grafts versus percutaneous coronary intervention for revascularization of high-risk patients. *Circulation* **114**, 1251-1257 (2006).

8. Cheneau, E., *et al.* Predictors of subacute stent thrombosis – Results of a systematic intravascular ultrasound study. *Circulation* **108**, 43-47 (2003).

9. Alfonso, F., *et al.* Findings of intravascular ultrasound during acute stent thrombosis. *Heart* **90**, 1455-1459 (2004).

10. Fujii, K., *et al.* Stent underexpansion and residual reference segment stenosis are related to stent thrombosis after sirolimus-eluting Stent implantation. *Journal of the American College Of Cardiology* **45**, 995-998 (2005).

11. Gutierrez-Chico, J.L., *et al.* Delayed Coverage in Malapposed and Side-Branch Struts With Respect to Well-Apposed Struts in Drug-Eluting Stents In Vivo Assessment With Optical Coherence Tomography. *Circulation* **124**, 612-623 (2011).

12. Goldstein, J.A., *et al.* Coronary Embolization Following Balloon Dilation of Lipid-Core Plaques. *JACC: Cardiovascular Imaging* **2**, 1420-1424 (2009).

13. Waxman, S., *et al.* A case of lipid core plaque progression and rupture at the edge of a coronary stent: Elucidating the mechanisms of drug-eluting stent failure. *Circulation: Cardiovascular Interventions.* **3**, 193-196 (2010).

14. Serruys, P.W., *et al.* Percutaneous Coronary Intervention versus Coronary-Artery Bypass Grafting for Severe Coronary Artery Disease. *New England Journal of Medicine* **360**, 961-972 (2009).

15. Stolker, J.M., *et al.* Repeat Revascularization After Contemporary Percutaneous Coronary Intervention. *Circulation: Cardiovascular Interventions* **5**, 772-782 (2012).

16. Taniwaki, M., *et al.* Four Year Clinical Outcomes and Predictors of Repeat Revascularization in Patients Treated With New Generation Drug-Eluting Stents in the RESOLUTE All Comers Randomized Trial. *Journal of the American College Of Cardiology.*

17. Waxman, S., *et al.* In Vivo Validation of a Catheter-Based Near-Infrared Spectroscopy System for Detection of Lipid Core Coronary Plaques: Initial Results of the SPECTACL Study. *Journal of the American College Of Cardiology: Cardiovascular Imaging* **2**, 858-868 (2009).

18. Jansen, K., *et al.* Spectroscopic intravascular photoacoustic imaging of lipids in atherosclerosis. *Journal of biomedical optics* **19**, 026006 (2014).

19. Tearney, G.J., *et al.* Images in cardiovascular medicine. Catheter-based optical imaging of a human coronary artery. *Circulation* **94**, 3013 (1996).

20. Tearney, G.J., *et al.* Scanning single-mode fiber optic catheter-endoscope for optical coherence tomography. *Optics letters* **21**, 543-545 (1996).

21. Tearney, G.J., *et al.* In vivo endoscopic optical biopsy with optical coherence tomography. *Science* **276**, 2037-2039 (1997).

22. Yabushita, H., *et al.* Characterization of human atherosclerosis by optical coherence tomography. *Circulation* **106**, 1640-1645 (2002).

23. Tearney, G.J., *et al.* Consensus standards for acquisition, measurement, and reporting of intravascular optical coherence tomography studies: a report from the International Working Group for Intravascular Optical Coherence Tomography Standardization and Validation. *Journal of the American College Of Cardiology* **59**, 1058-1072 (2012).

24. Prati, F., *et al.* Angiography alone versus angiography plus optical coherence tomography to guide decision-making during percutaneous coronary intervention: the Centro per la Lotta contro l'Infarto-Optimisation of Percutaneous Coronary Intervention (CLI-OPCI) study. *EuroIntervention* **8**, 823-829 (2012).

25. Kume, T., *et al.* Measurement of the thickness of the fibrous cap by optical coherence tomography. *American Heart Journal* **152**, 755 e751-754 (2006).

26. Falk, E. Plaque rupture with severe pre-existing stenosis precipitating coronary thrombosis. Characteristics of coronary atherosclerotic plaques underlying fatal occlusive thrombi. *British Heart Journal.* **50**, 127-134 (1983).

27. Serruys, P.W., *et al.* A bioabsorbable everolimus-eluting coronary stent system (ABSORB): 2-year outcomes and results from multiple imaging methods. *Lancet* **373**, 897-910 (2009).

28. Huang, D., *et al.* Optical coherence tomography. *Science* **254**, 1178-1181 (1991).

29. Chinn, S.R., Swanson, E.A. & Fujimoto, J.G. Optical coherence tomography using a frequency-tunable optical source. *Optics letters* **22**, 340-342 (1997).

30. Golubovic, B., Bouma, B.E., Tearney, G.J. & Fujimoto, J.G. Optical frequency-domain reflectometry using rapid wavelength tuning of a Cr4+:forsterite laser. *Optics letters* **22**, 1704-1706 (1997).

31. Yun, S., Tearney, G., de Boer, J., Iftimia, N. & Bouma, B. High-speed optical frequency-domain imaging. *Optics express* **11**, 2953-2963 (2003).

32. Huber, R., Adler, D.C. & Fujimoto, J.G. Buffered Fourier domain mode locking: Unidirectional swept laser sources for optical coherence tomography imaging at 370,000 lines/s. *Optics letters* **31**, 2975-2977 (2006).

33. Choma, M., Sarunic, M., Yang, C. & Izatt, J. Sensitivity advantage of swept source and Fourier domain optical coherence tomography. *Optics express* **11**, 2183-2189 (2003).

34. de Boer, J.F., *et al.* Improved signal-to-noise ratio in spectral-domain compared with time-domain optical coherence tomography. *Optics letters* **28**, 2067-2069 (2003).

35. Kawase, Y., *et al.* Comparison of nonuniform rotational distortion between mechanical IVUS and OCT using a phantom model. *Ultrasound in medicine & biology* **33**, 67-73 (2007).

36. Dufour, M.L., *et al.* Tools for experimental characterization of the non-uniform rotational distortion in intravascular OCT probes. *SPIE Proceeding*, **7883**, 788339 (2011).

37. Cho, H.S., *et al.* High frame-rate intravascular optical frequency-domain imaging in vivo. *Biomedical Optics Express* **5**, 223-232 (2013).

38. Okamura, T., Onuma, Y., Garcia-Garcia, H.M., Bruining, N. & Serruys, P.W. High-speed intracoronary optical frequency domain imaging: implications for three-dimensional reconstruction and quantitative analysis. *EuroIntervention* **7**, 1216-1226 (2012).

39. Farooq, V., *et al.* Three-dimensional optical frequency domain imaging in conventional percutaneous coronary intervention: the potential for clinical application. *European heart journal* **34**, 875-885 (2013).

40. van Ditzhuijzen, N.S., *et al.* The impact of Fourier-Domain optical coherence tomography catheter induced motion artefacts on quantitative measurements of a PLLA-based bioresorbable scaffold. *The international journal of cardiovascular imaging* (2014).

41. Kanda, T., *et al.* A micro ultrasonic motor using a micro-machined cylindrical bulk PZT transducer. *Sensors and Actuators A: Physical* **127**, 131-138 (2006).

42. Lee, S., Kim, D., Bryant, M.D. & Ling, F.F. A micro corona motor. *Sensors and Actuators A: Physical* **118**, 226-232 (2005).

43. Watson, B., Friend, J. & Yeo, L. Piezoelectric ultrasonic micro/milli-scale actuators. *Sensors and Actuators A: Physical* **152**, 219-233 (2009).

44. Chen, T., *et al.* Tiny endoscopic optical coherence tomography probe driven by a miniaturized hollow ultrasonic motor. *Journal of Biomedical Optics* **18**, 86011 (2013).

45. R. Erbel, T.R., L. Koch, J. Ge1, G. Görge, P. W. Serruys, N. Bom, C. T. Lancée and J. Roeland. IVUS of micromotors for cardiovascular imaging. *Minimally Invasive Therapy & Allied Technologies* (1997).

46. Charles T. Lancee, N.B. Ultrasonic instrument with a micro motor. *US Patent* (1994).

47. Pain, H.J. *The physics of vibrations and waves*, (WILEY, 1993).

48. Dill, R.B. Het Koppal van magnetische micromotoren met koperen en ijzeren statorlichamen. *Master thesis*, (1998).

49. Sarma, M.S. *Introduction to electrical engineering*, (Oxford university press, 2001).

50. D.j.dunn. *Instrumentation and control tutorial 2 – electric actuators*.

51. Ong, C.-M. *Dynamic simulation of electric machinery*, (Prentice hall PTR, 1998).

52. Nekoukar, V. & Erfanian, A. Adaptive terminal sliding mode control of ankle movement using functional electrical stimulation of agonist-antagonist muscles. *Conference proceedings : Annual International Conference of the IEEE Engineering in Medicine and Biology Society. IEEE Engineering in Medicine and Biology Society. Conference* **2010**, 5448-5451 (2010).

53. Wang, T.*, et al.* Intravascular optical coherence tomography imaging at 3200 frames per second. *Optics letters* **38**, 1715-1717 (2013).

54. Tsai, T.H.*, et al.* Ultrahigh speed endoscopic optical coherence tomography using micromotor imaging catheter and VCSEL technology. *Biomedical Optics Express* **4**, 1119-1132 (2013).

55. Swanson, E., Petersen, C.L., McNamaram, E., Lamport, R.B. & Kelly, D.L. Ultra-small optical probes, imaging optics, and methods for using same. in *U.S. Patent*, Vol. 6445939 (ed. LightLab Imaging, L.) (United States, 2002).

56. Regar, E., Ligthart, J., Bruining, N. & van Soest, G. The diagnostic value of intracoronary optical coherence tomography. *Herz* **36**, 417-429 (2011).

57. Okamura, T.*, et al.* First-in-man evaluation of intravascular optical frequency domain imaging (OFDI) of Terumo: a comparison with intravascular ultrasound and quantitative coronary angiography. *EuroIntervention* **6**, 1037-1045 (2011).

58. Huber, R., Wojtkowski, M. & Fujimoto, J.G. Fourier Domain Mode Locking (FDML): A new laser operating regime and applications for optical coherence tomography. *Optics express* **14**, 3225-3237 (2006).

59. Wieser, W., Biedermann, B.R., Klein, T., Eigenwillig, C.M. & Huber, R. Multi-megahertz OCT: High quality 3D imaging at 20 million A-scans and 4.5 GVoxels per second. *Optics express* **18**, 14685-14704 (2010).

60. Wieser, W.*, et al.* Extended coherence length megahertz FDML and its application for anterior segment imaging. *Biomedical Optics Express* **3**, 2647-2657 (2012).

61. Lancee, C.T., Bom, N. & Roelandt, J. Future directions in intravascular ultrasound: from micro-motors to imaging guidewire systems. *Echocardiography* **12**, 275-281 (1995).

62. Tran, P.H., Mukai, D.S., Brenner, M. & Chen, Z. In vivo endoscopic optical coherence tomography by use of a rotational microelectromechanical system probe. *Optics letters* **29**, 1236-1238 (2004).

63. Herz, P.R.*, et al.* Micromotor endoscope catheter for in vivo, ultrahigh-resolution optical coherence tomography. *Optics Letters* **29**, 2261-2263 (2004).

64. Li, J.*, et al.* High speed miniature motorized endoscopic probe for optical frequency domain imaging. *Optics Express* **20**, 24132-24138 (2012).

65. Adler, D.C.*, et al.* Three-dimensional endomicroscopy using optical coherence tomography. *Nature Photonics* **1**, 709-716 (2007).

66. Adler, D.C., Wieser, W., Trepanier, F., Schmitt, J.M. & Huber, R.A. Extended coherence length Fourier domain mode locked lasers at 1310 nm. *Optics Express* **19**, 20930-20939 (2011).

67. Witzenbichler, B.*, et al.* Relationship Between Intravascular Ultrasound Guidance and Clinical Outcomes After Drug-Eluting Stents: The Assessment of Dual Antiplatelet Therapy With Drug-Eluting Stents (ADAPT-DES) Study. *Circulation* **129**, 463-470 (2014).

68. Meneveau, N.*, et al.* Does optical coherence tomography optimize results of stenting? Rationale and study design. *Am Heart J* **168**, 175-181 e172 (2014).

69. Yun, S.H.*, et al.* Comprehensive volumetric optical microscopy in vivo. *Nature Medicine* **12**, 1429-1433 (2007).

70. Kang, W.*, et al.* Motion artifacts associated with in vivo endoscopic OCT images of the esophagus. *Optics Express* **19**, 20722-20735 (2011).

71. Tsai, T.H.*, et al.* Piezoelectric-transducer-based miniature catheter for ultrahigh-speed endoscopic optical coherence tomography. *Biomedical Optics Express* **2**, 2438-2448 (2011).

72. Biondi-Zoccai, G.G.L., *et al.* Incidence, predictors, and outcomes of coronary dissections left untreated after drug-eluting stent implantation. *European Heart Journal* **27**, 540-546 (2006).

73. Cook, S., *et al.* Incomplete Stent Apposition and Very Late Stent Thrombosis After Drug-Eluting Stent Implantation. *Circulation* **115**, 2426-2434 (2007).

74. Magro, M., *et al.* Residual atherothrombotic material after stenting in acute myocardial infarction – An optical coherence tomographic evaluation. *International Journal of Cardiology* **167**, 656-663 (2013).

75. Vlaar, P.J., *et al.* Cardiac death and reinfarction after 1 year in the Thrombus Aspiration during Percutaneous coronary intervention in Acute myocardial infarction Study (TAPAS): a 1-year follow-up study. *The Lancet* **371**, 1915-1920 (2008).

76. Yoo, H., *et al.* Intra-arterial catheter for simultaneous microstructural and molecular imaging in vivo. *Nature Medicine* **17**, 1680-1684 (2011).

77. Villiger, M., *et al.* Spectral binning for mitigation of polarization mode dispersion artifacts in catheter-based optical frequency domain imaging. *Optics Express* **21**, 16353-16369 (2013).

78. Li, X., Ko, T.H. & Fujimoto, J.G. Intraluminal fiber-optic Doppler imaging catheter for structural and functional optical coherence tomography. *Optics Letters* **26**, 1906-1908 (2001).

79. van Soest, G., *et al.* Atherosclerotic tissue characterization in vivo by optical coherence tomography attenuation imaging. *Journal of Biomedical Optics* **15**, 011105 (2010).

80. Kennedy, B.F., Kennedy, K.M. & Sampson, D.D. A Review of Optical Coherence Elastography: Fundamentals, Techniques and Prospects. *IEEE Journal of Selected Topics in Quantum Electronics.* **20**(2014).

81. van Velthoven, M.E.J., Faber, D.J., Verbraak, F.D., van Leeuwen, T.G. & de Smet, M.D. Recent developments in optical coherence tomography for imaging the retina. *Progress in Retinal and Eye Research.* **26**, 57-77 (2007).

82. Fu, H.L., *et al.* Flexible miniature compound lens design for high-resolution optical coherence tomography balloon imaging catheter. *Journal of Biomedical Optics* **13**, 060502 (2008).

83. Lamouche, G., *et al.* Intravascular optical coherence tomography on a beating heart model. *Journal of Biomedical Optics* **15**, 046023 (2010).

84. Li, X., Chudoba, C., Ko, T., Pitris, C. & Fujimoto, J.G. Imaging needle for optical coherence tomography. *Optics Letters* **25**, 1520-1522 (2000).

85. Tearney, G.J., *et al.* Scanning single-mode fiber optic catheter-endoscope for optical coherence tomography. *Optics Letters* **21**, 543-545 (1996).

86. Vakoc, B.J., *et al.* Comprehensive esophageal microscopy by using optical frequency–domain imaging (with video). *Gastrointestinal Endoscopy* **65**, 898-905 (2007).

87. van der Meer, F.J., Faber, D.J., Cilesiz, I., van Gemert, M.J. & van Leeuwen, T.G. Temperature-dependent optical properties of individual vascular wall components measured by optical coherence tomography. *Journal of Biomedical Optics* **11**, 041120 (2006).

88. Tearney, G.J., Jang, I.K. & Bouma, B.E. Optical coherence tomography for imaging the vulnerable plaque. *Journal of Biomedical Optics* **11**, 021002 (2006).

89. Brown, E.N., *et al.* Thinking inside the graft: applications of optical coherence tomography in coronary artery bypass grafting. *Journal of Biomedical Optics* **12**, 051704 (2007).

90. Bouma, B.E., *et al.* Evaluation of intracoronary stenting by intravascular optical coherence tomography. *Heart* **89**, 317-320 (2003).

91. Barlis, P., van Soest, G., Serruys, P.W. & Regar, E. Intracoronary optical coherence tomography and the evaluation of stents. *Expert Review of Medical Devices* **6**, 157-167 (2009).

92. van Soest, G., *et al.* Pitfalls in Plaque Characterization by OCT. *Journal of the American College Of Cardiology: Cardiovascular Imaging* **4**, 810-813 (2011).

93. Dufour, M.L., *et al.* Tools for experimental characterization of the non-uniform rotational distortion in intravascular OCT probes. *SPIE proceeding*, Vol. 7883 788339 (2011).

94. Tumlinson, A.R., Hariri, L.P., Utzinger, U. & Barton, J.K. Miniature endoscope for simultaneous optical coherence tomography and laser-induced fluorescence measurement. *Applied Optics* **43**, 113-121 (2004).

95. Meemon, P., Lee, K.S., Murali, S. & Rolland, J. Optical design of a dynamic focus catheter for high-resolution endoscopic optical coherence tomography. *Applied Optics* **47**, 2452-2457 (2008).

96. Xi, J., *et al.* High-resolution OCT balloon imaging catheter with astigmatism correction. *Optics Letters* **34**, 1943-1945 (2009).

97. Kang, W., *et al.* Endoscopically guided spectral-domain OCT with double-balloon catheters. *Optics Express* **18**, 17364-17372 (2010).

98. Drexler, W. & Fujimoto, J.G. (eds.). *Optical Coherence Tomography: Technology and Applications*, (Springer, 2008).

99. Yaqoob, Z., Wu, J., McDowell, E.J., Heng, X. & Yang, C. Methods and application areas of endoscopic optical coherence tomography. *Journal of Biomedical Optics* **11**, 063001 (2006).

100. Mao, Y., Chang, S., Sherif, S. & Flueraru, C. Graded-index fiber lens proposed for ultrasmall probes used in biomedical imaging. *Applied Optics* **46**, 5887-5894 (2007).

101. Jung, W., *et al.* Numerical analysis of gradient index lens-based optical coherence tomography imaging probes. *Journal of Biomedical Optics* **15**, 066027 (2010).

102. Silfvast, W.T. *Laser Fundamentals*, (Cambridge University Press, Cambridge UK, 2003).

103. Gomez, C.R., Perez, M.V. & Bao, C. (eds.). *Gradient-Index Optics*, (Springer, 2002).

104. Reno, C.W., CHill, C. & J., N. Laser astigmatism compensation. in *U.S. Patent* (United States, 1993).

105. Liu, X., Cobb, M.J., Chen, Y., Kimmey, M.B. & Li, X. Rapid-scanning forward-imaging miniature endoscope for real-time optical coherence tomography. *Optics Letters* **29**, 1763-1765 (2004).

106. Ha, J.Y., *et al.* Compensation of motion artifacts in catheter-based optical frequency domain imaging. *Optics express* **18**, 11418-11427 (2010).

107. Ha, J., Yoo, H., Tearney, G.J. & Bouma, B.E. Compensation of motion artifacts in intracoronary optical frequency domain imaging and optical coherence tomography. *The international journal of cardiovascular imaging* **28**, 1299-1304 (2012).

108. Wijns, W., *et al.* Guidelines on myocardial revascularization: The Task Force on Myocardial Revascularization of the European Society of Cardiology (ESC) and the European Association for Cardio-Thoracic Surgery (EACTS). *European heart journal* **31**, 2501-2555 (2010).

Heartbeat optical coherence tomography

1) Light is faster than sound. (this thesis)

2) Current clinical OCT is too slow to escape cardiac motion but too fast to be corrected for it. (this thesis)

3) High-speed rotational scanning uniformity in imaging catheters benefits from using a micro motor. (this thesis)

4) A torque measured in Nano-Newton-meter can be useful in a macroscopic mechanism system. (this thesis)

5) The catheter tube in IV-OCT introduces astigmatism that may be corrected for better image quality. (this thesis)

6) A "Fantastic Voyage" can be realized by using endoscopic imaging catheters rather than shrinking us.

7) A drawing means a thousand words while a diagnostic image is worth a thousand measurements.

8) He who loves practice without theory is like the sailor who boards ship without a rudder and compass and never knows where he may cast. (Leonardo da Vinci)

9) Miracles sometimes occur, but one has to work terribly hard for them. (C. Weizmann)

10) Working with 'Echte Rotterdammers' is the best way to become 'een Echte Rotterdammer'.

11) 地势坤，君子以厚德载物。(周易)
As earth's condition is receptive devotion, a gentle man should hold the outer world with broad mind. (Zhou Yi: Classic of change)

Curriculum Vitae

Tianshi Wang (王天时) was born on November 30th, 1983 in Liaoning, China. He obtained his Bachelor and Master degrees of Science in Physics from Tsinghua University, China. In 2010, he joined Thoraxcenter, Erasmus MC, University Medical Center Rotterdam to pursue his PhD degree. Here he conducted the research described in this thesis.